Article

Cell Reports

Defective Mitochondrial Pyruvate Flux Affects Cell Bioenergetics in Alzheimer's Disease-Related Models

Graphical Abstract

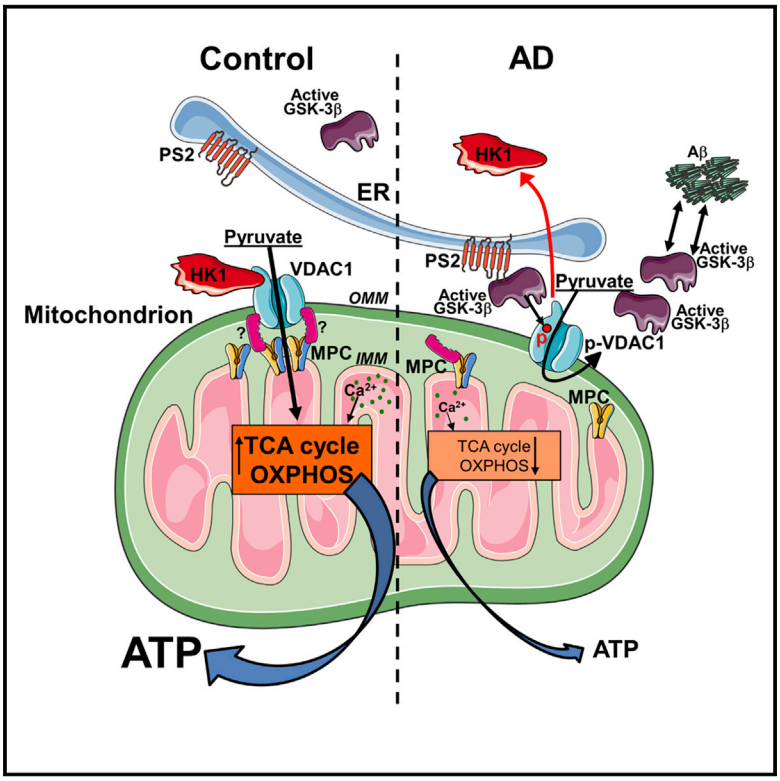

Highlights

- Mitochondrial ATP synthesis is reduced in Alzheimer's disease cell models
- Lower mitochondrial Ca^{2+} signal and pyruvate uptake impair cell bioenergetics
- GSK-3β reduces HK1-mitochondria association, destabilizing MPC complexes
- The defective mitochondrial pyruvate flux alters neuronal function

Authors

Alice Rossi, Giulia Rigotto, Giulia Valente, Valentina Giorgio, Emy Basso, Riccardo Filadi, Paola Pizzo

Correspondence

riccardo.filadi@unipd.it (R.F.), paola.pizzo@unipd.it (P.P.)

In Brief

Mitochondria are key organelles for brain health. Rossi et al. show that, in different Alzheimer's disease cell models, lower mitochondrial Ca^{2+} signal and pyruvate uptake reduce ATP synthesis. GSK-3β hyper-activation contributes to the defect by impairing HK1-mitochondria association, decreasing MPC2 levels and destabilizing MPC complexes. Defective bioenergetics affects neuronal functionality.

Rossi et al., 2020, Cell Reports *30*, 2332–2348
February 18, 2020
https://doi.org/10.1016/j.celrep.2020.01.060

CellPress

OPEN ACCESS
CellPress

Cell Reports
Article

Defective Mitochondrial Pyruvate Flux Affects Cell Bioenergetics in Alzheimer's Disease-Related Models

Alice Rossi,[1,3] Giulia Rigotto,[1,4] Giulia Valente,[1,2] Valentina Giorgio,[1,2] Emy Basso,[1,2] Riccardo Filadi,[1,2,*] and Paola Pizzo[1,2,5,*]

[1]Department of Biomedical Sciences, University of Padua, Via U. Bassi 58/B, 35121 Padua, Italy
[2]Neuroscience Institute - Italian National Research Council (CNR), Padua 35121, Italy
[3]Present address: Department of Neuroscience, Max-Delbrück Centrum für Molekulare Medizin, Robert-Rössle-Str. 10, 13125 Berlin-Buch, Germany
[4]Present address: Department of Immunology and Molecular Oncology, Veneto Institute of Oncology, IOV-IRCCS, Padua 35121, Italy
[5]Lead Contact
*Correspondence: riccardo.filadi@unipd.it (R.F.), paola.pizzo@unipd.it (P.P.)
https://doi.org/10.1016/j.celrep.2020.01.060

SUMMARY

Mitochondria are key organelles for brain health. Mitochondrial alterations have been reported in several neurodegenerative disorders, including Alzheimer's disease (AD), and the comprehension of the underlying mechanisms appears crucial to understand their relationship with the pathology. Using multiple genetic, pharmacological, imaging, and biochemical approaches, we demonstrate that, in different familial AD cell models, mitochondrial ATP synthesis is affected. The defect depends on reduced mitochondrial pyruvate oxidation, due to both lower Ca^{2+}-mediated stimulation of the Krebs cycle and dampened mitochondrial pyruvate uptake. Importantly, this latter event is linked to glycogen-synthase-kinase-3β (GSK-3β) hyper-activation, leading, in turn, to impaired recruitment of hexokinase 1 (HK1) to mitochondria, destabilization of mitochondrial-pyruvate-carrier (MPC) complexes, and decreased MPC2 protein levels. Remarkably, pharmacological GSK-3β inhibition in AD cells rescues MPC2 expression and improves mitochondrial ATP synthesis and respiration. The defective mitochondrial bioenergetics influences glutamate-induced neuronal excitotoxicity, thus representing a possible target for future therapeutic interventions.

INTRODUCTION

In neurons, mitochondria are essential to produce ATP and sustain physiological synaptic activity, which involves a multitude of highly energy-demanding processes (Magistretti and Allaman, 2015). The major bioenergetic mitochondrial pathway, the Krebs (or tricarboxylic acid [TCA]) cycle, takes place in the matrix; here, it extracts electrons from carbon sources in the form of NADH and FADH2 and supplies them to the electron transport chain (ETC) for ATP production. Importantly, Ca^{2+} signal modulates the activity of multiple carriers (Del Arco et al., 2016) and stimulates different TCA cycle enzymes (Denton, 2009; Rossi et al., 2019), playing a key role in the regulation of mitochondrial metabolism. In neurons, Ca^{2+} entry within mitochondria regulates, in an activity-dependent fashion, their energy metabolism (Llorente-Folch et al., 2015). Indeed, neuronal activity not only consumes ATP but also promptly stimulates its synthesis (Rangaraju et al., 2014), a process driven by a tight association between mitochondrial Ca^{2+} oscillations and synaptic electrical activity.

The importance of a correct mitochondrial metabolism for brain health is highlighted by the finding of common, multiple mitochondrial alterations in major neurodegenerative diseases, such as Alzheimer's disease (AD), Parkinson's disease (PD), and amyotrophic lateral sclerosis (Golpich et al., 2017; Lin and Beal, 2006). Under stress conditions, defective mitochondrial metabolism can lead to an insufficient ATP production, which, in the long term, causes neuronal impairments and cell death (Federico et al., 2012; Pathak et al., 2015; Schon and Manfredi, 2003). Moreover, altered mitochondrial Ca^{2+} signaling has been consistently described in different neurological disorders (Calì et al., 2012; Celsi et al., 2009; Filadi et al., 2017). As far as AD is concerned, early alterations of intracellular Ca^{2+} homeostasis have been reported; though the underlying mechanisms are debated, there is consensus on their potential to deeply impact on AD pathophysiology (Agostini and Fasolato, 2016). In particular, mutant forms of presenilin 2 (PS2), linked to familial cases of AD (FAD) (Haass and Selkoe, 2007), dampen mitochondrial Ca^{2+} rises upon cell stimulations (Filadi et al., 2016; Kipanyula et al., 2012; Zampese et al., 2011), as a consequence of a lower amount of Ca^{2+} available within the endoplasmic reticulum (ER) (Brunello et al., 2009; Giacomello et al., 2005; Greotti et al., 2016; Kipanyula et al., 2012; Zatti et al., 2004, 2006).

Starting from these observations, we here evaluated, in different FAD-PS2 models, mitochondrial bioenergetics and found a lower ATP synthesis. Mechanistically, FAD-PS2 mutants affect mitochondrial activity partly by altering mitochondrial Ca^{2+} signaling and partly by inducing a glycogen-synthase-kinase-3β (GSK-3β)-dependent detachment of hexokinase 1 (HK1) from mitochondria. We found that this latter event, of utmost

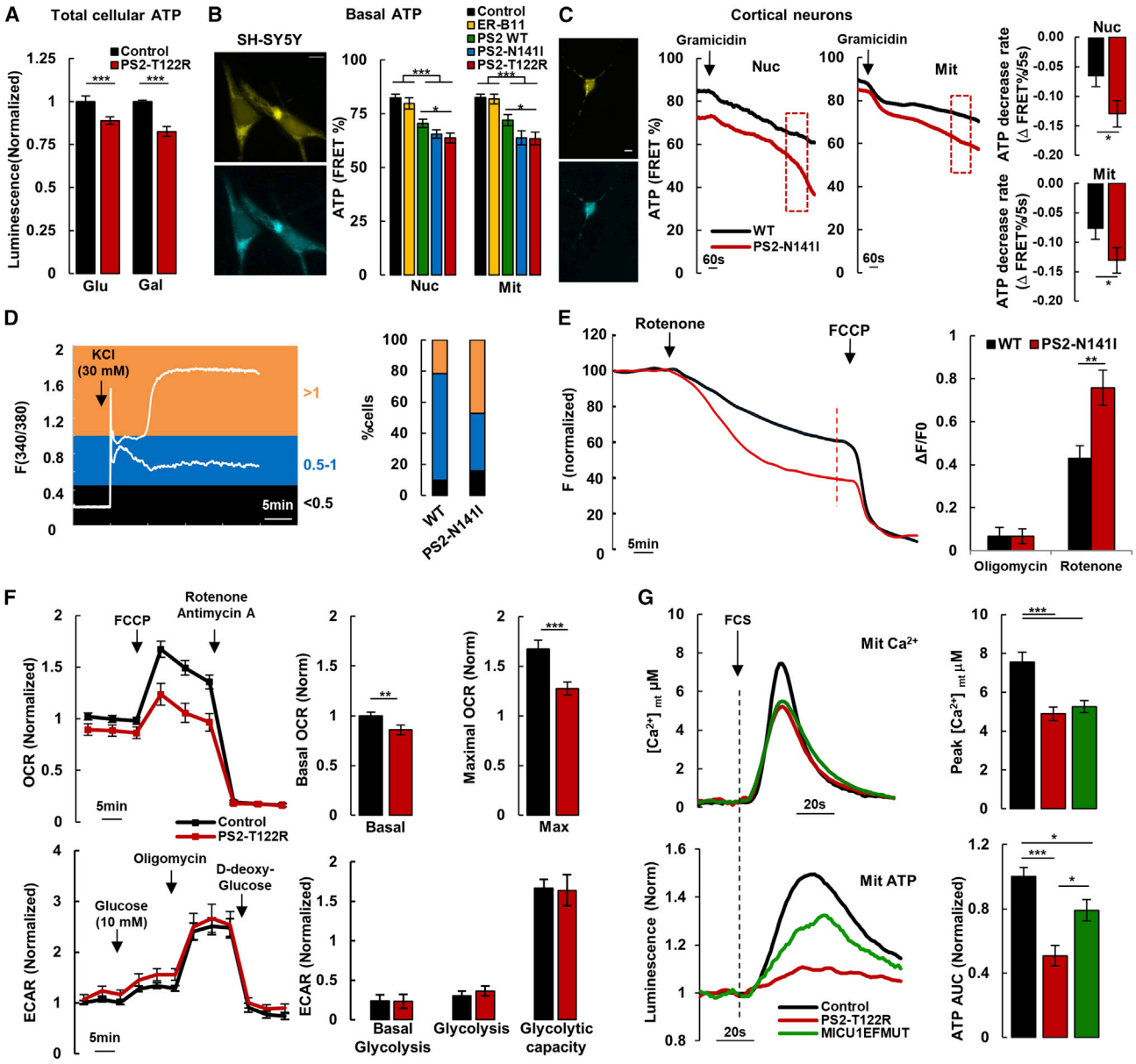

Figure 1. FAD-PS2 Expression Decreases Mitochondrial ATP Production, Partly by Reducing Mitochondrial Ca^{2+} Signaling

(A) Total cellular ATP levels (see STAR Methods) in control (pcDNA3) and PS2-T122R-expressing SH-SY5Y cells, grown either in glucose (Glu)- or galactose (Gal)-containing medium. n = 42–90 wells from 4 independent experiments.

(B) Representative images (YFP and CFP channels, left) and mean FRET % values (proportional to [ATP]) of nuclear (Nuc) and mitochondrial (Mit) ATeam1.03 probes in control, ER-β11-, PS2 WT-, PS2-T122R-, or PS2-N141I-expressing SH-SY5Y cells, grown in galactose-containing medium. n = 41–65 cells, 15–19 coverslips from 3 independent experiments. Scale bar, 10 μm.

(C) Representative images and traces of ATP dynamics in primary cortical neurons of WT and PS2-N141I-tg mice (days *in vitro* [DIV] 6), transfected with both Nuc and Mit ATeam1.03. Where indicated, gramicidin (0.3 μM) was added. On the right, bars represent the mean decrease rate of Nuc- and Mit-ATP measured for 3 min, after 15 min from gramicidin addition (dotted boxes on traces). n = 30 cells, 24–26 coverslips from 3 independent experiments. Scale bar, 10 μm.

(D) Left: representative traces of Ca^{2+} dynamics measured with Fura-2 in primary hippocampal neurons of WT and PS2-N141I-tg mice (DIV 10–12), exposed to KCl. 20 min after KCl exposure, $[Ca^{2+}]_{cyt}$ recovery was evaluated, grouping cells for their 340/380 ratio (right; see STAR Methods). n = 3 independent experiments.

(E) Left: representative traces of TMRM fluorescence measured in primary hippocampal neurons of WT and PS2-N141I-tg mice (DIV 10–12). Where indicated, rotenone (1 μM) was added. Right: bars represent the mean drop of TMRM fluorescence (ΔF/F0) measured 20 min after exposure to either rotenone (1 μM) or oligomycin (2 μg/mL). Fluorescence intensity was normalized to basal values. n = 10–22 cells, 6–10 coverslips from 3 independent experiments.

(F) Traces (left) represent the mean OCR (top) or extracellular acidification rate (ECAR) (bottom) in control and PS2-T122R-expressing SH-SY5Y cells, grown in galactose-containing medium. FCCP (0.5 μM), rotenone (1 μM), antimycin-A (0.1 μM), glucose (10 mM), oligomycin (1 μg/mL), and D-deoxy-glucose (20 mM) were

(legend continued on next page)

importance for the metabolic coordination of the cell (Robey and Hay, 2006; Shoshan-Barmatz and Mizrachi, 2012), affects protein stability of the mitochondrial-pyruvate-carrier-2 (MPC2) and impairs mitochondrial pyruvate uptake. Finally, we demonstrated that the bioenergetic imbalance contributes to a known hallmark of AD, i.e., glutamate-induced neuronal excitotoxicity, rescued by overcoming the defective mitochondrial pyruvate uptake.

RESULTS

FAD-PS2 Expression Decreases Mitochondrial ATP Production

We tested whether FAD-PS2 expression affects a key mitochondrial activity, i.e., ATP synthesis. First, we evaluated overall ATP levels in human neuroblastoma cells (SH-SY5Y): compared to controls, FAD-PS2-T122R-expressing cells showed a decreased total ATP content when grown in either glucose-containing or glucose-free, galactose-containing medium (Figure 1A). Galactose for glucose replacement forces mitochondrial ATP synthesis (Figure S1A), highlighting possible mitochondrial defects (Gohil et al., 2010). We then compared the effects of wild-type (WT)- and FAD-PS2 expression on ATP concentrations, because elevated levels of WT PS2 have been demonstrated to induce similar, although milder, cell alterations compared to those triggered by FAD-PS2 (Fedeli et al., 2019; Giacomello et al., 2005; Zampese et al., 2011; Zatti et al., 2004) and an increased expression of endogenous WT PS2 has been found in prefrontal cortex of sporadic AD patients (Lu et al., 2014). By employing targeted fluorescence resonance energy transfer (FRET)-based ATP probes (nuclear and mitochondrial ATeam1.03; Imamura et al., 2009), reduced basal ATP levels were observed in both nucleus (that mirrors cytosolic ATP dynamics; Imamura et al., 2009) and mitochondrial matrix of living WT PS2-, FAD-PS2-T122R-, or FAD-PS2-N141I-expressing SH-SY5Y cells (with a stronger effect of FAD-PS2 mutants; Figures 1B and S1B). A similar ATP reduction was observed in mouse embryonic fibroblasts (MEFs) (Figure S1C), suggesting that the effect of FAD-PS2 is cell type independent. Importantly, ATP concentration was not affected by the expression of a non-fluorescent GFP fragment targeted to ER membranes (ER- β11) (Figure 1B; see STAR Methods), thus excluding possible unspecific effects due to protein overexpression. To investigate the mechanisms underlying these PS2-induced bioenergetic alterations, we focused on FAD-PS2 mutants, whose expression induces the larger effects. In accordance with ATP measurements, an increased phosphorylation of the energy sensor protein, AMP-activated protein kinase (AMPK) (Garcia and Shaw, 2017) was detected in PS2-T122R-expressing cells, compared to controls (Figure S1D).

The observed lower ATP levels could result from reduced synthesis or increased usage. However, control and FAD-PS2-expressing cells, treated with oligomycin to block the ATP synthase, displayed similar rates of ATP decay (both in the nucleus and within mitochondria; Figure S1E), suggesting a similar consumption in the two cell types.

We then investigated ATP dynamics in primary cortical neurons from WT and FAD-PS2-N141I transgenic (tg) mice. In resting conditions, no significantly different ATP levels were observed between the two genotypes (Figures 1C and S1F). However, when we challenged neurons with low doses of gramicidin-A, to force the activity of Na^+/K^+ ATPase and ATP consumption (Figure S1G; Brand and Nicholls, 2011; Filadi et al., 2018), the drop in both nuclear and mitochondrial ATP levels was more pronounced in FAD-PS2-N141I neurons (Figure 1C). Importantly, to evaluate mitochondrial ATP production independently of glycolysis, in these experiments, cells were bathed in a medium containing pyruvate as the only carbon source, suggesting that FAD-linked mutants specifically affect mitochondrial functionality.

A reduced capacity to synthetize ATP under stress conditions could affect cell Ca^{2+} handling, tightly controlled by the activity of different ATPases (Zampese and Pizzo, 2012). WT and FAD-PS2-N141I hippocampal neurons were exposed to KCl (30 mM), a stimulus known to induce cell depolarization and a strong cytosolic Ca^{2+} increase. Compared to controls, a larger proportion of FAD-PS2-N141I neurons was unable to recover basal Ca^{2+} levels after KCl addition and underwent cytosolic Ca^{2+} overload (Figure 1D), further suggesting a possible impairment of cell bioenergetics.

To get insights into the mechanisms underlying these subtle defects, we investigated the activity of ETC and ATP synthase in both intact cells and isolated mitochondria. Mitochondrial membrane potential ($\Delta\psi$) was assessed by tetramethylrhodamine methyl ester (TMRM) in primary hippocampal neurons from WT and FAD-PS2-N141I-tg mice (Figure 1E). Upon complex I inhibition (by rotenone), a faster $\Delta\psi$ decay was observed in FAD-PS2 neurons compared to WT cells, although, by inhibiting ATP synthase (with oligomycin), no significant alterations in $\Delta\psi$ were observed (Figure 1E). Reasoning that, whenever the ETC is inhibited, the reverse activity of ATP synthase can consume ATP to sustain $\Delta\psi$, a faster $\Delta\psi$ drop, upon rotenone addition, may indicate an intrinsically defective reverse activity or a lower ATP availability, though a possible impact of increased reactive oxygen species (due to respiratory chain inhibition) on ATP synthase and/or permeability transition pore cannot be excluded. Importantly, however, ATP synthase reverse activity was not significantly different in brain-isolated mitochondria from WT and FAD-PS2-N141I-tg mice (Figure S1H; Luvisetto et al., 1987). Moreover, in brain-isolated mitochondria,

added, as indicated. After measurements, data were normalized for cell number and to control baseline OCR. Bars (right) represent the mean basal and maximal (after FCCP addition) OCR (top) or ECAR (bottom) for the indicated conditions (see STAR Methods). n = 22–36 wells from 4 independent experiments.
(G) Representative traces, mean peak $[Ca^{2+}]_{mt}$, and area under the curve (AUC) values of mitochondrial Ca^{2+} uptake (top) and ATP production (bottom) in control, PS2-T122R-, and $MICU1_{EFMUT}$-expressing SH-SY5Y cells grown in galactose-containing medium and expressing either mitochondrial matrix aequorin or luciferase. Cells were stimulated by acute exposure to fetal calf serum (FCS) (3%). n = 11–31 coverslips from 3 independent experiments.
Mean ± SEM. *p < 0.05; **p < 0.01; ***p < 0.001.
See also Figures S1 and S2.

measurements of $\Delta\psi$ (Figure S1I) and respiration (Figure S1J) did not reveal any significant difference between the two genotypes. The expression levels of the different ETC complexes and ATP synthase resulted unchanged in hippocampal neurons from WT and FAD-PS2-N141I-tg mice (Figure S1K). In agreement, FAD-PS2-T122R expression in SH-SY5Y cells did not significantly alter the expression levels of these proteins (Figure S2A) but induced lower basal and maximal (Figure 1F), as well as ATP-linked (Figure S2B), oxygen consumption rates (OCRs), in face of similar proton leak (Figure S2B) and glycolytic activity (Figure 1F). Though basal and maximal OCRs were reduced upon FAD-PS2 expression (Figure 1F), the specific contribution of complex I and complex II activity to the respective maximal OCR was similar in control and FAD-PS2-expressing cells (Figure S2C). In line with these observations, maximal OCR has been found to be lower in intact cortical neurons from FAD-PS2-N141I/APP_{swe} tg mice, compared to WT cells (Theurey et al., 2019). Overall, these data suggest that the cellular energetic context, rather than intrinsic organelle defects, alters mitochondrial activity in the presence of FAD-PS2.

The FAD-PS2-Induced Bioenergetic Impairment Is Partly Due to a Dampened Mitochondrial Ca^{2+} Signaling

Physiological mitochondrial Ca^{2+} rises are known to sustain ATP synthesis (Denton, 2009; Rossi et al., 2019), and FAD-PS2 mutants have been shown to dampen ER Ca^{2+} content (Brunello et al., 2009; Filadi et al., 2016; Giacomello et al., 2005; Greotti et al., 2016; Kipanyula et al., 2012; Zampese et al., 2011; Zatti et al., 2004, 2006), affecting ER to mitochondria Ca^{2+} transfer (Filadi et al., 2016; Kipanyula et al., 2012; Zampese et al., 2011). Accordingly, upon acute stimulation of ER Ca^{2+} release with the inositol trisphosphate (IP3)-generating agonist bradykinin (BK), FAD-PS2-T122R-expressing cells displayed reduced mitochondrial Ca^{2+} peaks (Figure S2D). We therefore tested whether these alterations in mitochondrial Ca^{2+} handling are responsible for organelle defective activity. A rapid mitochondrial ATP rise was observed following BK-cell stimulation (Figure S2D), as previously reported (Jouaville et al., 1999) and in line with the key role of mitochondrial Ca^{2+} signal on ATP synthesis (Bell et al., 2006; Jouaville et al., 1999; Wiederkehr et al., 2011). In FAD-PS2-T122R-expressing cells, however, much lower BK-stimulated ATP increases, compared to controls, were observed (Figure S2D), possibly due to the reduced mitochondrial Ca^{2+} uptake in these cells. Because BK triggers maximal IP3-dependent ER Ca^{2+} release, we tested, in a more physiological condition, the impact of serum (FCS [fetal calf serum]) addition on mitochondrial Ca^{2+} uptake and ATP synthesis. Indeed, it has been demonstrated that a low, constitutive IP3-dependent ER to mitochondria Ca^{2+} transfer, promoted by growth factors present in the serum, sustains mitochondrial bioenergetics (Cárdenas et al., 2010; Filadi et al., 2018). We found that FCS stimulates mitochondrial Ca^{2+} rises and ATP production, with lower effects in FAD-PS2-T122R-expressing cells (Figure 1G). Importantly, FCS-induced mitochondrial Ca^{2+} uptake depends on ER Ca^{2+} release and not to Ca^{2+} entry from the plasma membrane (PM), because it was observed also in a Ca^{2+}-free, EGTA-containing medium (Figure S2E). Similar results were obtained in HT-22 mouse hippocampal neuronal cells (Figure S2F). In line with the reduced mitochondrial Ca^{2+} uptake, higher levels of phosphorylated pyruvate dehydrogenase (P-PDH) (the inactive form) were observed in FAD-PS2-T122R-expressing SH-SY5Y cells (Figure S2G).

The FAD-PS2-induced alterations in mitochondrial Ca^{2+} uptake were then mimicked in control cells either genetically (Figure 1G), by overexpressing a mutant form of the regulatory protein Mitochondrial Calcium Uptake 1 ($MICU1^{EFmut}$) that reduces the activity of the mitochondrial calcium uniporter (MCU) complex (Patron et al., 2014), or pharmacologically (Figure S2H), by partially inhibiting sarco-endoplasmic reticulum calcium ATPase (SERCA) activity pre-treating cells with sub-maximal doses of cyclopiazonic acid (CPA), thus reducing ER Ca^{2+} content (Filadi et al., 2016; Zampese et al., 2011). Compared to controls, both approaches induced a reduction in mitochondrial ATP synthesis following FCS cell stimulation (Figures 1G and S2H). However, in FAD-PS2-expressing cells, despite similar mitochondrial Ca^{2+} rises, the decrease in ATP production was larger (Figures 1G and S2H), suggesting that mitochondrial Ca^{2+} alterations are only partially responsible for the bioenergetic defect induced by the mutated protein and that additional mechanisms are involved.

Defective Pyruvate Utilization and Reduced Association of Hexokinase 1 with Mitochondria Affect Mitochondrial Bioenergetics in FAD-PS2-Expressing Cells

Mitochondrial activity is sustained by the cytosolic *milieu*, providing different substrates, which, once transported in the matrix, feed TCA cycle and ETC (Taylor, 2017). We thus speculated that an insufficient availability of specific nutrients within mitochondria may contribute to their defective activity. In particular, the TCA cycle can be fueled mainly by three substrates (Figure 2A): pyruvate; fatty acids; and glutamine/glutamate (Currie et al., 2013; DeBerardinis et al., 2008; Frezza, 2017; Olson et al., 2016; Vacanti et al., 2014; Yang et al., 2014). By specifically inhibiting each of these routes (Vacanti et al., 2014), we compared the effects on OCR, in control and FAD-PS2-T122R-expressing SH-SY5Y cells. We found that each specific treatment marginally influences basal OCR (Figures 2Bi–2Biv) but largely affects maximal OCR in both control and FAD-PS2-T122R-expressing cells (Figures 2Bi–2Biv), with faint responses to FCCP compared to untreated cells (Figure 2B). These results suggest that mitochondria, under stress conditions, need to exploit different substrates to maintain their optimal activity. Importantly, in FAD-PS2-T122R-expressing cells, maximal OCR remained lower than in controls by blocking either fatty acids or glutamine utilization (Figures 2Biii and 2Biv), as observed in untreated cells (Figure 2Bi). However, by inhibiting the pyruvate route, no difference in this parameter was anymore observed between the two cell types (Figure 2Bii). Overall, these data indicate that FAD-PS2 expression specifically affects mitochondrial pyruvate utilization. A similar conclusion was reached also by inhibiting each pathway and comparing, in control and FAD-PS2-T122R-expressing cells exposed to low doses of gramicidin (see above and STAR Methods), the effects on ATP levels (Figure S2I). As observed in neurons (Figure 1C), we found that gramicidin induces a larger ATP drop in FAD-PS2-expressing cells compared to control (Figure S2I). This difference was maintained by inhibiting either the fatty acids or the glutamate

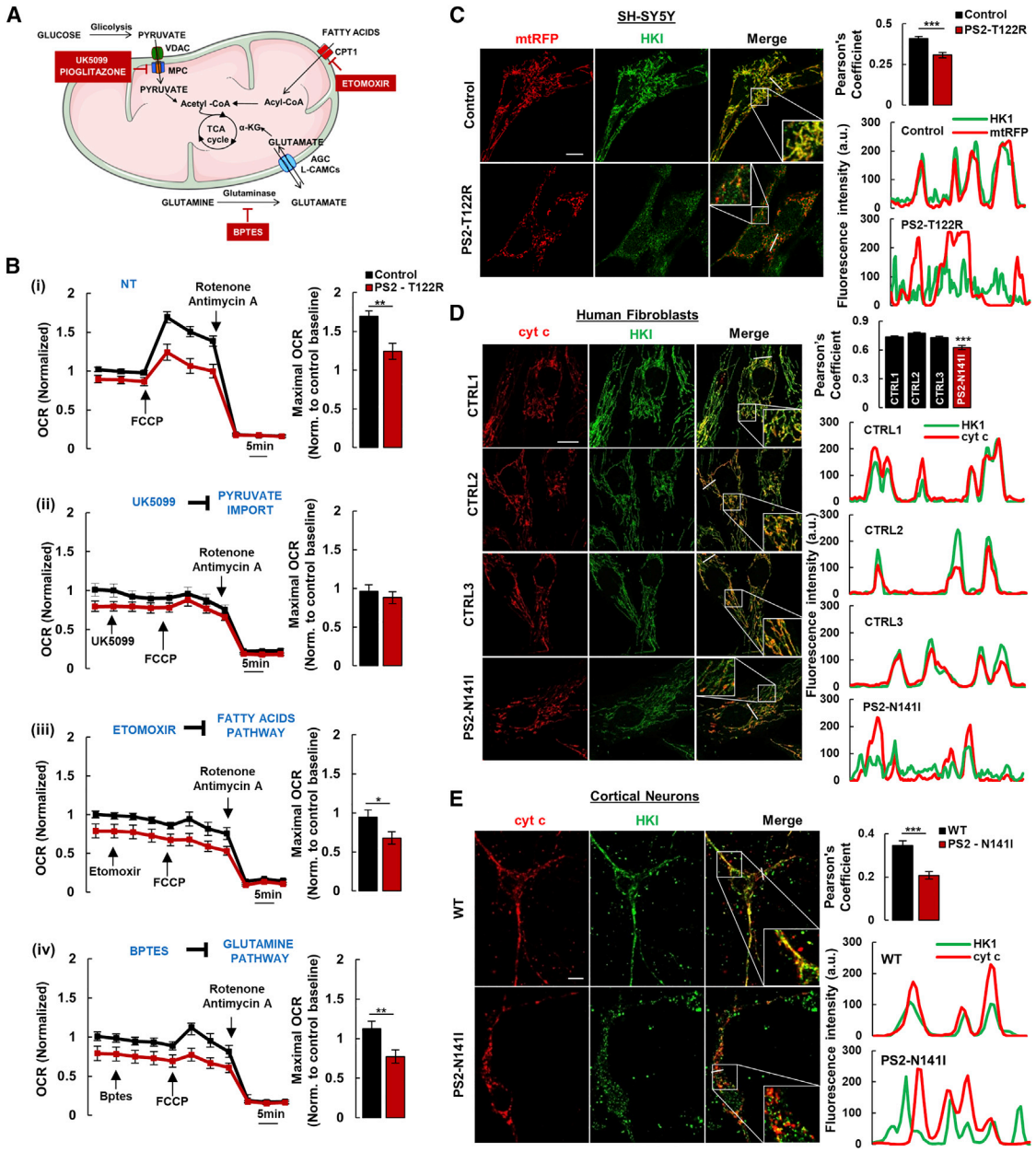

Figure 2. FAD-PS2-Expressing Cells Show an Impairment of Mitochondrial Pyruvate Metabolism and a Decreased HK1-Mitochondria Association

(A) The cartoon represents the three main metabolic pathways feeding TCA cycle and their respective inhibitors.

(B) Traces represent mean OCR in control and PS2-T122R-expressing cells grown in galactose-containing medium and treated as indicated (NT, not treated). On the right, bars represent the maximal OCR (upon FCCP exposure) for each specific condition. n = 15–20 wells from 3 independent experiments.

(C–E) Representative confocal images of SH-SY5Y cells (C), human fibroblasts (D), and mouse cortical neurons (E) expressing a mitochondrial RFP (mtRFP) (C) or immunostained for cytochrome *c* (D and E) and endogenous HK1 (C–E). On the right, Pearson's co-localization coefficients between HK1 signal and the respective mitochondrial markers are shown. Traces represent red and green fluorescence intensity along the linear regions of interest (ROIs) traced in the merge images to visualize signal co-distribution. Scale bars, 10 μm.

(C) SH-SY5Y cells, co-transfected with mtRFP and either pcDNA3 (control) or PS2-T122R cDNAs. n = 56–57 cells, 8 coverslips from 4 independent experiments.

(D) Fibroblasts from three healthy controls (CTRL 1, 2, 3) and a FAD-PS2-N141I patient. n = 37–58 cells, 6 coverslips from 3 independent experiments.

(E) Primary cortical neurons (DIV 11) from WT and PS2-N141I-tg mice. n = 39–46 cells, 9 coverslips from 3 independent experiments.

Mean ± SEM. *p < 0.05; ***p < 0.001.

See also Figure S3.

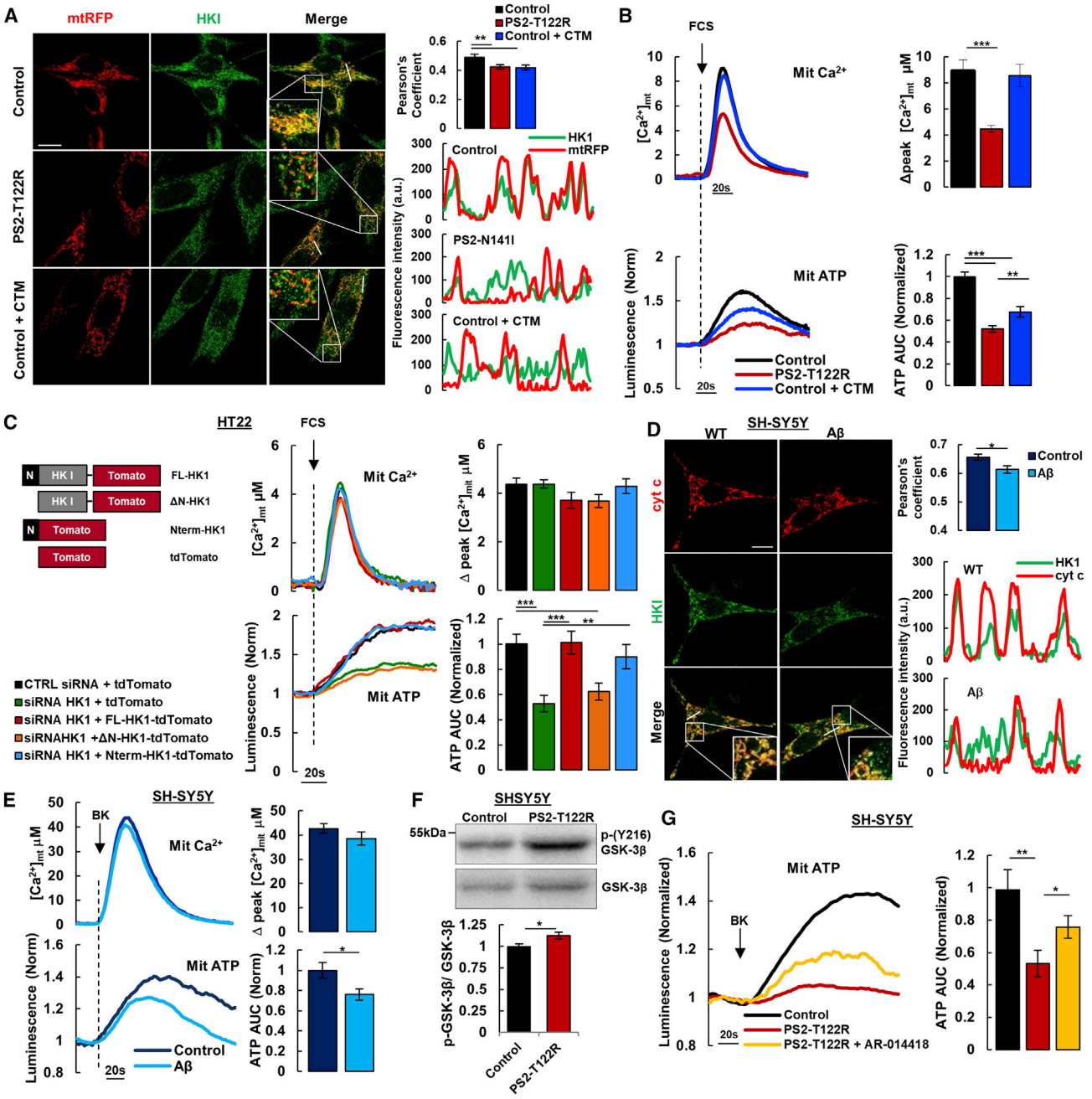

Figure 3. FAD-PS2 Expression Affects Mitochondrial Bioenergetics by Altering HK1-Mitochondria Association

(A) Representative confocal images of SH-SY5Y cells expressing mtRFP and immunostained for endogenous HK1. Pearson's co-localization coefficients and signal co-distributions (as in Figure 2C) for each condition are shown on the right. CTM (5 μM; 10 min). n = 35–39 cells, 6 coverslips from 3 independent experiments. Scale bar, 10 μm.

(B) Representative traces, mean peaks $[Ca^{2+}]_{mt}$ (top), and AUC values for mitochondrial ATP production (bottom) in control, CTM-treated control, and PS2-T122R-expressing SH-SY5Y cells, measured as in Figure 1G. n = 5–19 coverslips from 3 independent experiments.

(C) Representative traces and mean values (right) of mitochondrial Ca^{2+} (top panels) and ATP (bottom panels) rises in HT-22 cells, grown in galactose-containing medium and co-transfected with cDNAs for mitochondrial luciferase or aequorin and either cytosolic tdTomato, full-length HK1-tdTomato (FL-HK1), truncated-HK1-tdTomato (ΔN-HK1), or Nterm-HK1-tdTomato, together with either scramble siRNA (CTRL siRNA) or HK1-specific siRNA, as indicated. Cells were stimulated with FCS (3%). n = 12–35 coverslips from 4 independent experiments.

(D) Representative confocal images of SH-SY5Y cells treated overnight with a conditioned medium collected from either WT Chinese hamster ovary (CHO) (control) or FAD-APP-V717F-expressing CHO7PA2 (Aβ) cells, immunostained for cytochrome *c* and endogenous HK1. Pearson's co-localization coefficients and signal co-distributions (as in Figure 2D) are shown on the right. n = 52–53 cells, 9 wells from 3 independent experiments. Scale bar, 10 μm.

(legend continued on next page)

pathway, but not upon inhibition of the pyruvate route (Figure S2I). Importantly, the drugs used to evaluate the contribution of each metabolic pathway, i.e., UK5099 to inhibit mitochondrial pyruvate uptake (see also below Figures S4A and S4B), BPTES to inhibit glutaminase, and etomoxir to inhibit carnitine-palmitoyltransferase-I (CPT1) (and thus lipids transfer to mitochondria; Figure S2J), were used acutely (see STAR Methods) and did not significantly affect mitochondrial abundance (Figure S2K).

Of note, pyruvate holds a crucial metabolic branch point, because it bridges glycolysis and mitochondrial oxidative phosphorylation. Indeed, once produced by glycolysis in the cytosol, part of pyruvate is transported within mitochondria, crossing the outer mitochondrial membrane (OMM) through the voltage-dependent anion channel (VDAC) (Shoshan-Barmatz et al., 2018) and the inner mitochondrial membrane (IMM) through the MPC (Bricker et al., 2012; Herzig et al., 2012). Importantly, the dynamic association of HK (the first enzyme of glycolysis) with the OMM (in particular with VDAC1; Pastorino and Hoek, 2008; Robey and Hay, 2006) is known to modulate the metabolic coupling between cytosol and mitochondria by regulating both glycolysis and oxidative phosphorylation. We thus tested the extent of HK1 (the isoform expressed in the brain; Robey and Hay, 2006) association with mitochondria in our AD cell models. A lower HK1-mitochondria co-localization was observed in FAD-PS2-T122R-expressing SH-SY5Y cells, compared to controls (Figure 2C), in primary human fibroblasts from a FAD-PS2-N141I patient, compared to those from three healthy controls (Figure 2D), and in primary cortical neurons from FAD-PS2-N141I tg mice, compared to WT cells (Figure 2E). Importantly, comparable HK1 protein levels were found in the different FAD models and their respective controls (Figure S3A; Table S1), and the expression of VDAC1 (the putative HK1 mitochondrial receptor) is not affected by the presence of FAD-PS2 mutants (Filadi et al., 2016).

By mimicking in control cells, either pharmacologically or genetically, HK1 detachment from mitochondria, as observed in our AD models, we obtained a similar bioenergetic impairment. Treatments of control SH-SY5Y cells with low doses of clotrimazole (CTM), a drug reported to detach HK from mitochondria (Chiara et al., 2008), decreased HK1-mitochondria interaction to levels similar to those observed in FAD-PS2-expressing cells (Figure 3A; Video S1) and dampened FCS-induced mitochondrial ATP production (Figure 3B, bottom), without affecting mitochondrial Ca^{2+} uptake (Figure 3B, top), $\Delta\psi$ (Figure S3B), or HK1 expression (Table S1). The additional drop in ATP peaks, observed in PS2-T122R-expressing cells (Figure 3B), may be due to the specific effect of FAD-PS2 mutants on Ca^{2+} transfer to mitochondria. Importantly, the decreased ATP production upon CTM treatment was not due to ATP synthase reverse activity (to sustain mitochondrial $\Delta\psi$), as verified by TMRM fluorescence measurements in cells treated with oligomycin (to block its activity) and exposed to CTM (Figure S3C). These results suggest that HK1-mitochondria association modulates ATP synthesis.

We further investigated this aspect genetically, by knocking down (KD) endogenous HK1 and re-expressing different chimeric, small interfering RNA (siRNA)-resistant HK1 forms (Figure 3C) in HT-22 cells, chosen as cell model because of the high efficiency of HK1-KD (Figure S3D). We found that HK1-KD impairs FCS-stimulated mitochondrial ATP rises (Figure 3C, green trace/bar) and the re-expression of full-length HK1 (FL-HK1) (Figure S3D), which predominantly associates with mitochondria (Figure S3E), rescues this defect (Figure 3C, red trace/bar). On the other hand, the re-expression of a cytosolic HK1 form (ΔN-HK1; Figures S3D and S3E), which conserves the enzymatic activity (Sun et al., 2008) but lacks the N-terminal peptide (14 amino acids) necessary for its binding to mitochondria, does not recover the defect in ATP synthesis (Figure 3C, orange trace/bar). Interestingly, the expression of the N-terminal, 14 amino acid peptide (Nterm-HK1) alone, which binds to mitochondria (Figure S3E) but lacks the catalytic domain (Sun et al., 2008), was sufficient to fully rescue ATP production (Figure 3C, cyan trace/bar). Of note, none of the above genetic manipulations affected FCS-induced mitochondrial Ca^{2+} uptake (Figure 3C, upper traces/panels). Moreover, the expression of each of these three constructs, together with control-siRNA, did not affect ATP synthesis (Figure S3F), excluding possible unspecific effects. These data strongly indicate that HK1 binding to mitochondria sustains organelle ATP synthesis independently of its enzymatic activity and mitochondrial Ca^{2+} signaling, suggesting that the lower HK1-mitochondria association, observed in AD cell models (Figures 2C–2E), may contribute to the reduced bioenergetics in addition to the altered Ca^{2+} homeostasis.

Remarkably, exposure of control SH-SY5Y cells to a conditioned medium from FAD-APP-V717F-expressing CHO7PA2 cells (containing naturally occurring Aβ oligomers in the low nM range; Hedskog et al., 2013; Figure S3G), compared to a conditioned medium from WT CHO cells, decreased HK1-mitochondria co-localization (Figure 3D) to a similar extent of that observed in FAD-PS2-expressing cells and affected BK-induced ATP rises (Figure 3E, bottom), without changing mitochondrial Ca^{2+} response (Figure 3E, top) or HK1 expression (Table S1). This suggests that different alterations commonly observed in AD, such as an impaired Aβ generation/clearance, may converge on this pathway, possibly extending the significance of our findings also to sporadic AD.

It has been demonstrated that the binding of HK1 to mitochondria may be inhibited by the phosphorylation of VDAC1 (i.e., its

(E) Representative traces and mean values of mitochondrial Ca^{2+} and ATP rises in SH-SY5Y cells (measured as in B) treated as in (D). Cells were stimulated by BK (100 nM). n = 20–22 coverslips from 3 independent experiments.

(F) Representative western blot and quantification of p-(Y216)-GSK-3β and total GSK-3β in control and PS2-T122R-expressing SH-SY5Y cells. n = 5 independent experiments.

(G) Representative traces and AUC quantification of mitochondrial ATP production in control and PS2-T122R-expressing SH-SY5Y cells treated, or not, with AR-A014418 (100 nM; 16 h). Cells were stimulated by BK (100 nM). n = 7–15 coverslips from 3 independent experiments.

Mean ± SEM. *p < 0.05; **p < 0.01; ***p < 0.001.

See also Figure S3.

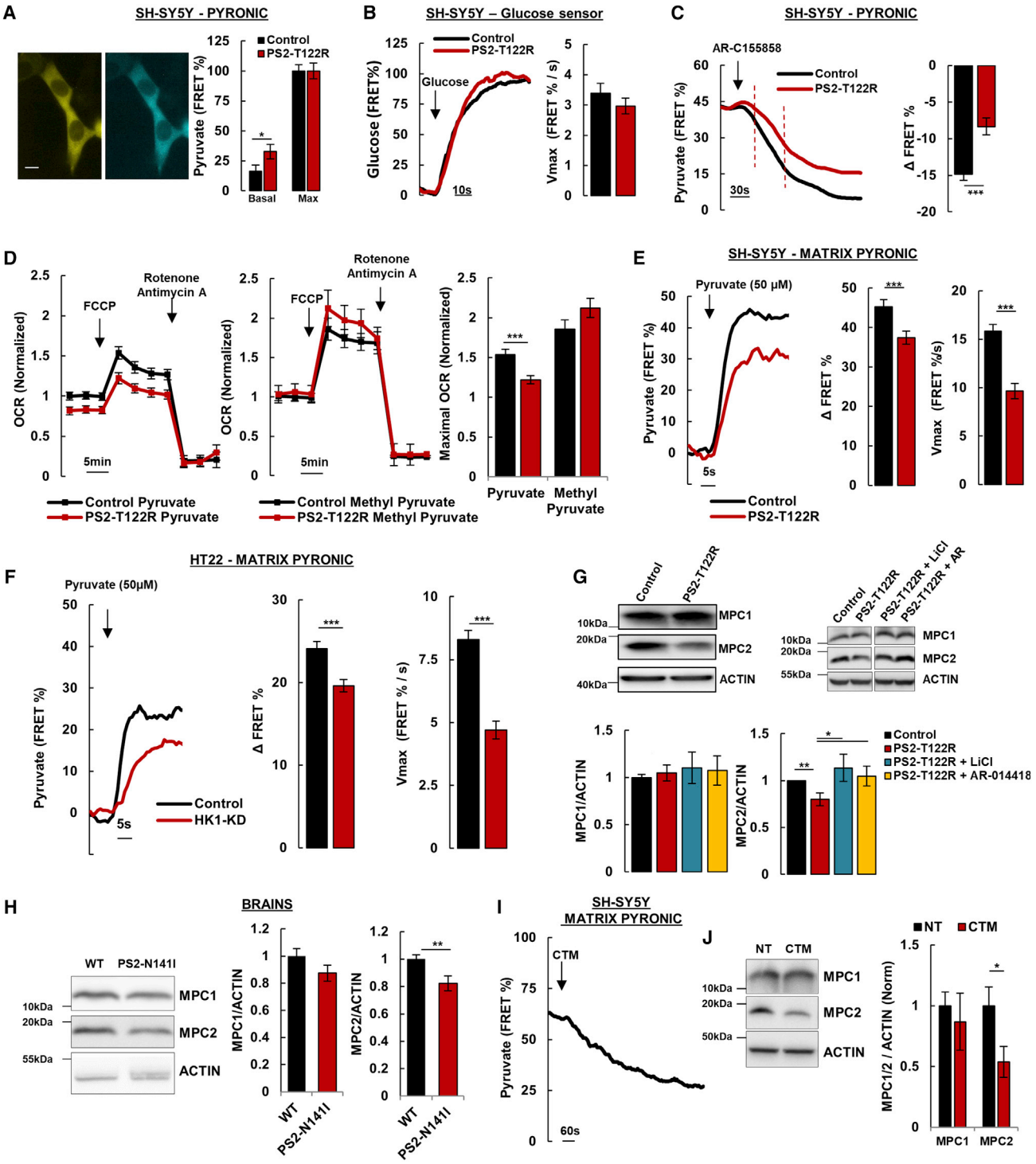

Figure 4. Reduced HK1-Mitochondria Association in FAD-PS2-Expressing Cells Affects Mitochondrial Pyruvate Import

(A) Representative images and mean FRET % (proportional to [pyruvate]) of Pyronic probe in control and PS2-T122R-expressing SH-SY5Y cells, bathed in glucose-containing medium (see STAR Methods). n = 19–29 cells, 9–12 coverslips from 3 independent experiments. Scale bar, 10 μm.

(B) Representative traces (left) and mean Vmax values of ΔFRET % of the FLII12Pglu-700uDelta6 glucose probe (see STAR Methods) in control and PS2-T122R-expressing SH-SY5Y cells, exposed to glucose where indicated (1 mM). n = 23–29 cells, 7–8 coverslips from 3 independent experiments.

(legend continued on next page)

putative receptor on the OMM; Robey and Hay, 2006) mediated by GSK-3β (Pastorino et al., 2005). Importantly, GSK-3β has been consistently reported to be hyper-activated in AD (Leroy et al., 2007; Llorens-Martín et al., 2014; Qin et al., 2006) and responsible for *tau* hyper-phosphorylation, a typical hallmark of the disease (Kremer et al., 2011). We thus speculated that FAD-PS2 might trigger HK1 detachment from mitochondria through GSK-3β hyper-activation. Indeed, higher levels of GSK-3β, phosphorylated at tyrosine 216 (pY-216) (the active form of the enzyme), were observed in FAD-PS2-T122R-expressing SH-SY5Y cells (Figure 3F), as previously reported in several other AD models (Leroy et al., 2007; Llorens-Martín et al., 2014; Qin et al., 2006). Interestingly, treatment with either AR-A014418 (Bhat et al., 2003) or LiCl (Freland and Beaulieu, 2012), two completely different GSK-3β inhibitors, partially recovered BK-stimulated ATP synthesis (Figures 3G and S3H), as well as OCR (Figure S3I), in FAD-PS2-T122R-expressing SH-SY5Y cells, suggesting that this pathway may be involved in the observed effects.

A Reduced Hexokinase1-Mitochondria Association in FAD-PS2-Expressing Cells Causes a Defective Mitochondrial Pyruvate Import

As to the mechanism by which FAD-PS2, modulating HK1-mitochondria interaction, affects ATP synthesis, we observed that FAD-PS2 expression impairs the capacity of mitochondria to utilize efficiently pyruvate as substrate (Figures 2B and S2I). We therefore wondered whether insufficient mitochondrial pyruvate availability could be involved in the observed alterations. By employing a FRET-based pyruvate probe (Pyronic; San Martín et al., 2014), higher cytosolic pyruvate levels were retrieved in FAD-PS2-T122R-expressing cells in resting conditions (Figure 4A). Interestingly, glucose uptake was not significantly modified by FAD-PS2 expression (Figure 4B) or by glycolysis (Figure 1F), suggesting that the increased cytosolic pyruvate concentration may arise from a lower mitochondrial pyruvate uptake or utilization rather than a higher synthesis. To investigate mitochondrial pyruvate flux, glucose-deprived cells were first exposed to pyruvate, leading to its prompt entry through PM-located monocarboxylate transporters (MCTs) (San Martín et al., 2014) and achieving equal cytosolic levels between control and FAD-PS2-T122R-expressing cells (Figure 4C). Then, cells were treated with a specific MCT inhibitor (AR-C155858; Ovens et al., 2010), decreasing cytosolic pyruvate levels due to the ongoing mitochondrial pyruvate uptake and oxidation (San Martín et al., 2014; Figure 4C). A slower decrease in the FRET signal was observed in FAD-PS2-T122R-expressing cells compared to controls (Figure 4C), further suggesting an impaired mitochondrial pyruvate metabolism.

To investigate the mechanism underlying this reduced mitochondrial pyruvate flux, OCR was measured in cells bathed with a medium containing pyruvate (that needs specific transporters to reach the mitochondrial matrix; Figures S4A and S4B) or methyl-pyruvate (that freely permeates through both the OMM and the IMM; Figures S4A and S4B; see also STAR Methods). A specific pyruvate concentration (100 μM) was added to the medium to attain cytosolic pyruvate levels similar to those physiologically observed when glucose is available (Figure S4C). Although, compared to controls, basal and maximal OCR were lower in FAD-PS2-T122R-expressing SH-SY5Y cells supplemented with pyruvate (Figure 4D, left traces and histogram), the defects were completely rescued upon cell exposure to methyl-pyruvate (Figure 4D, right traces and histogram), suggesting a defective metabolite uptake as responsible for the reduced mitochondrial activity. We thus directly monitored mitochondrial pyruvate influx. First, we tested whether FAD-PS2, by detaching HK1 from mitochondria, changes the permeability of the OMM to this substrate. Pyruvate concentrations in the mitochondrial inter-membrane space (MIMS) were measured in cells expressing a MIMS-located Pyronic probe (Figure S4D; see STAR Methods). Similar MIMS pyruvate dynamics were observed in control and FAD-PS2-expressing cells (Figure S4E). On the other hand, by testing IMM permeability by a mitochondrial matrix-targeted Pyronic (Figure S4F; see STAR Methods), a slower and lower pyruvate uptake, compared to controls, was found in FAD-PS2-expressing cells (Figure 4E), as well as upon HK1-KD (Figure 4F).

(C) Representative traces of Pyronic FRET % in control and FAD-PS2-T122R-expressing SH-SY5Y cells, bathed in a pyruvate (0.3 mM)-containing medium. Where indicated, AR-C166868 (1.5 μM) was added. On the right, bars represent the mean decrease in the FRET signal after 30 s (interval within the dotted red lines) from AR-C155858 addition. n = 56–64 cells, 14–15 coverslips from 3 independent experiments.

(D) Mean traces of OCR in control and PS2-T122R-expressing SH-SY5Y cells, bathed in a medium containing either pyruvate (0.1 mM, left) or methyl-pyruvate (2 mM, middle panel) and treated as indicated. On the right, bars represent mean maximal OCR for the indicated conditions. n = 21–35 wells from 4 independent experiments.

(E) Representative traces, mean values, and Vmax of ΔFRET % of the mitochondrial matrix-targeted Pyronic probe in control and FAD-PS2-T122R-expressing SH-SY5Y cells upon addition of pyruvate (50 μM; see STAR Methods and Figure S4F). n = 55–66 cells, 16–18 coverslips from 3 independent experiments.

(F) Mitochondrial pyruvate uptake, measured as in (E), in HT-22 cells transfected with either control or HK1-specific siRNAs (HK1-KD). n = 89–116 cells, 22–23 coverslips from 4 independent experiments.

(G and H) Representative western blots and quantification of endogenous MPC1 and MPC2 expression levels (normalized to actin) in (G) control and PS2-T122R-expressing SH-SY5Y cells, treated or not with LiCl (10 mM; 16 h) or AR-014418 (100 nM; 16 h; n = 5–10 independent experiments), and (H) brain lysates from WT and PS2-N141I-tg mice (n = 16 independent experiments).

(I) Representative trace of pyruvate dynamics (expressed as FRET %) in SH-SY5Y cells expressing the mitochondrial matrix-targeted Pyronic, bathed in a medium supplemented with pyruvate (100 μM). Where indicated, CTM (5 μM) was added to induce HK1 detachment from mitochondria. n = 26 cells, 9 coverslips from 3 independent experiments.

(J) Representative western blot and quantification of MPC1 and MPC2 expression levels in SH-SY5Y cells, treated or not (NT) with CTM (5 μM) for 6 h. n = 4 independent experiments.

Mean ± SEM. *$p < 0.05$; **$p < 0.01$; ***$p < 0.001$.

See also Figure S4.

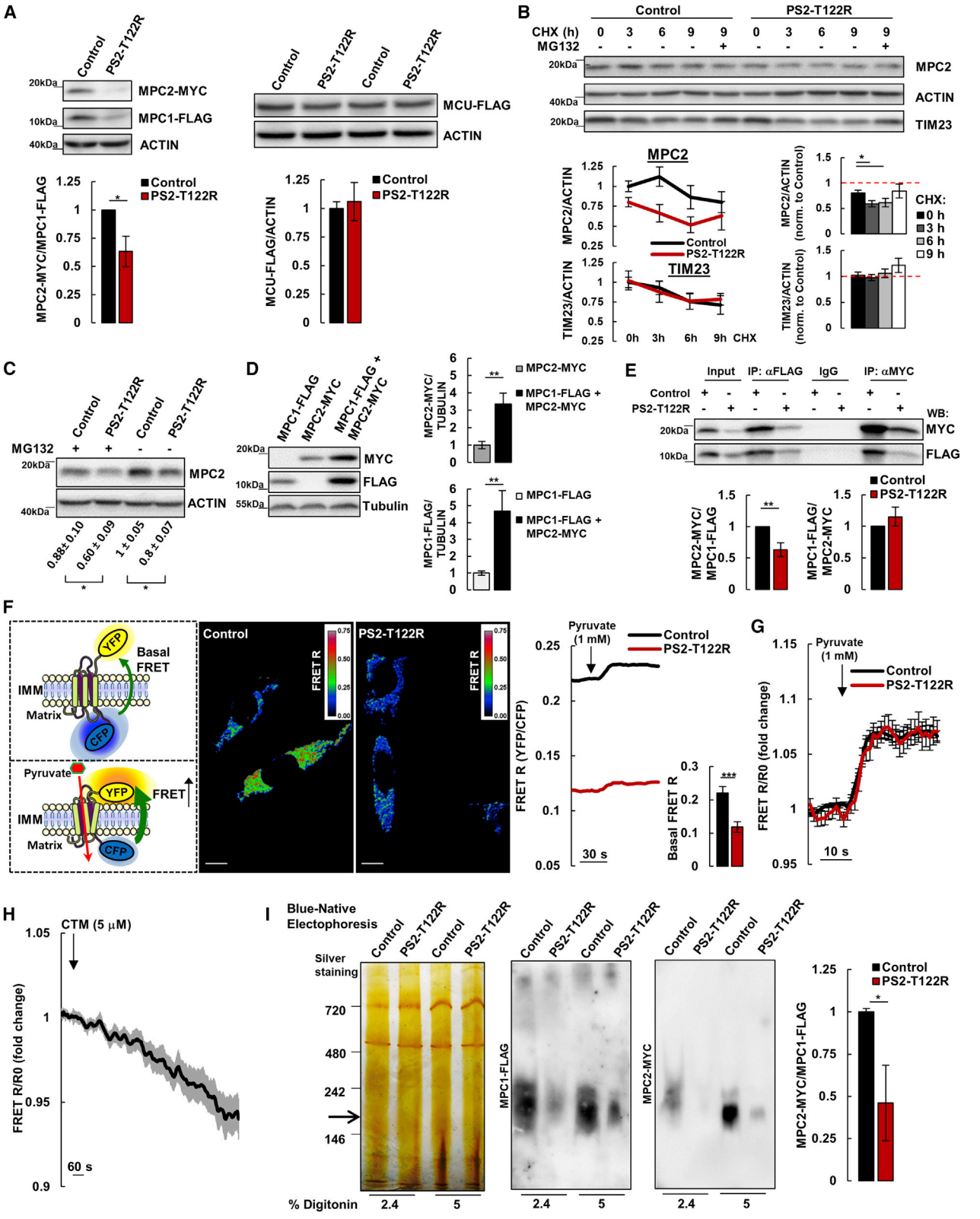

(legend on next page)

We thus checked the expression levels of MPC1 and MPC2, the two MPC subunits that assemble into functional oligomers (Bricker et al., 2012; Herzig et al., 2012). Interestingly, in FAD-PS2-T122R-expressing SH-SY5Y cells, compared to controls, similar MPC1 but lower MPC2 levels were observed (Figure 4G). Similar alterations were present in brain lysates from FAD-PS2-N141I-tg mice compared to WT animals (Figure 4H). Importantly, GSK-3β inhibition in FAD-PS2-expressing cells, which improves mitochondrial ATP production and respiration (Figures 3G, S3H, and S3I), rescued MPC2 expression (Figure 4G). Of note, in SH-SY5Y cells, acute CTM treatment, which detaches HK1 from mitochondria and reduces ATP synthesis (Figures 3A and 3B), dampened mitochondrial pyruvate uptake (Figure 4I), and, after 6 h, reduced MPC2, but not MPC1, levels (Figure 4J). Similarly, HK1-KD reduced MPC2 expression (Figure S4G).

The FAD-PS2-induced lower MPC2 expression may depend on alterations in gene transcription or protein stability. The expression levels of exogenous (i.e., under the control of a CMV promoter) MPC2-MYC and, to a lower extent, of MPC1-FLAG (Figure 5A, left), but not those of MCU-FLAG (as an IMM-located control protein; Figure 5A, right), were lower in SH-SY5Y cells co-expressing FAD-PS2-T122R, thus excluding a transcriptional control at the endogenous promoter of the *MPC2* gene. On the other hand, a faster degradation of endogenous MPC2, but not of TIM23 (the translocase of the IMM subunit 23, evaluated as an IMM-located control protein), was observed after 3 and 6 h of cycloheximide-induced inhibition of protein synthesis in FAD-PS2-expressing SH-SY5Y cells compared to controls (Figure 5B). Of note, the increased MPC2 degradation rate was independent from proteasome activity, because it was not recovered by MG132 treatment (Figures 5B and 5C). Interestingly, when we co-expressed together MPC2-MYC and MPC1-FLAG, their respective protein levels were considerably higher compared to those found in cells transfected with either MPC2-MYC or MPC1-FLAG expression-plasmids alone (Figure 5D), possibly suggesting that the reported MPC1-MPC2 assembly into functional hetero-oligomers (Bender et al., 2015; Bricker et al., 2012; Herzig et al., 2012) stabilizes these proteins, avoiding their degradation. We therefore speculated that FAD-PS2, by detaching HK1 from the OMM, may destabilize MPC1-MPC2 complexes, increasing MPC2 degradation. Crossed co-immunoprecipitation experiments revealed that, compared to controls, in FAD-PS2-expressing SH-SY5Y cells, a lower proportion of MPC2-MYC was co-precipitated by MPC1-FLAG, although a similar proportion of MPC1-FLAG was co-precipitated by MPC2-MYC (Figure 5E). These results suggest that, likely because of the decreased MPC2/MPC1 ratio observed in FAD-PS2-expressing cells (Figure 5A), a lower fraction of MPC1 is engaged in the formation of functional hetero-complexes with MPC2, but the MPC2 pool is complexed with MPC1. To evaluate MPC1-MPC2 assembly and activity in living cells, we modified a previously reported genetically encoded, bioluminescence resonance energy transfer (BRET)-based MPC-activity biosensor (Compan et al., 2015) into a FRET-based probe (see STAR Methods; Figure 5F). We observed a lower basal FRET ratio between MPC1-CFP and MPC2-YFP in FAD-PS2-expressing cells compared to controls (Figure 5F), suggesting a reduced MPC hetero-complex assembly. In line with results obtained previously with the reported BRET probe (Compan et al., 2015), pyruvate addition induced a small but significant increase in the FRET signal (Figure 5F, traces), likely because of changes in MPC conformation during pyruvate transport. However, when we compared the pyruvate-induced fold increase of the FRET ratios in control and FAD-PS2-expressing cells (taking into account the different basal FRET values; see STAR Methods), we observed similar changes in the two cell types (Figure 5G). Overall, these data suggest that, in FAD-PS2-expressing cells, though less MPC1-MPC2 hetero-complexes are formed, those that assemble are functional. Importantly, acute CTM treatment reduced the FRET signal between MPC1-CFP and MPC2-YFP (Figure 5H), suggesting that HK1-mitochondria association modulates MPC1-MPC2 assembly. Finally, blue-native electrophoresis of mitochondrial extracts confirmed that, in FAD-PS2-T122R-expressing SH-SY5Y cells, a lower amount of ~180–200 kDa MPC1-MPC2 hetero-complexes are formed (Figure 5I).

The Altered Mitochondrial Bioenergetics in FAD-PS2-Expressing Cells Worsens Glutamate-Dependent Neuronal Ca^{2+} Excitotoxicity

Neuronal excitotoxicity mediated by an exaggerated post- and extra-synaptic Ca^{2+} influx through N-methyl-d-aspartate ionotropic L-glutamate receptors (NMDAR) has been consistently

Figure 5. FAD-PS2 Expression Affects MPC2 Protein Stability and the Assembly of MPC1-MPC2 Hetero-complexes

(A–E) Representative western blots and quantification of (A) MPC1-FLAG and MPC2-MYC (left) or MCU-FLAG (right) expression in control and FAD-PS2-T122R-expressing SH-SY5Y cells, n = 6 independent experiments; (B and C) endogenous MPC2 (B and C) and TIM23 (B) expression in control and FAD-PS2-T122R-expressing SH-SY5Y cells, treated with cycloheximide (CHX) (50 μg/mL) and/or MG132 (10 μM), as indicated; bottom (B) traces (left) represent the relative MPC2 or TIM23 levels for each time point in control and FAD-PS2-T122R-expressing cells; bars (right) represent MPC2 or TIM23 levels in FAD-PS2-T122R-expressing cells normalized, at each time point, to those of controls (highlighted by the dotted red line), n = 4 independent experiments; (D) MPC1-FLAG and MPC2-MYC expression in SH-SY5Y cells, transfected with either MPC1-FLAG or MPC2-MYC cDNAs alone or co-transfected with both cDNAs, n = 4 independent experiments; and (E) co-immunoprecipitation experiments, performed with the specified antibodies in control or FAD-PS2-T122R-expressing SH-SY5Y cells, co-transfected with both MPC1-FLAG and MPC2-MYC cDNAs. Precipitates (immunoprecipitation [IP]) and total lysates (input) were probed with the indicated antibodies. n = 5 independent experiments.

(F) Representative images (middle), traces (right), and mean basal values of FRET R (YFP/CFP fluorescence; inset) in control and FAD-PS2-T122R-expressing SH-SY5Y cells, co-expressing MPC1-CFP and MPC2-YFP. n = 35–53 cells, 18–21 coverslips from 3 independent experiments. Left: the cartoon represents the functionality of the probe. Scale bars, 10 μm.

(G and H) Traces represent the average fold change of the FRET R upon pyruvate (G) or CTM (H) addition in, respectively, control and FAD-PS2-T122R-expressing (G) or in control SH-SY5Y cells (H), co-expressing MPC1-CFP and MPC2-YFP. FRET R at each time point was normalized to the initial value (R0). n = 31–53 cells, 15–21 coverslips from 3 independent experiments.

(I) Representative blue native gel (silver staining, left) and corresponding western blots of native protein extracts from mitochondria of control and FAD-PS2-T122R-expressing SH-SY5Y cells, co-expressing MPC1-FLAG and MPC2-MYC. Bars represent the ratio between MPC2-MYC and MPC1-FLAG in the ~180-kDa protein-complex for the indicated conditions. n = 3 independent experiments. Mean ± SEM. *p < 0.05; **p < 0.01.

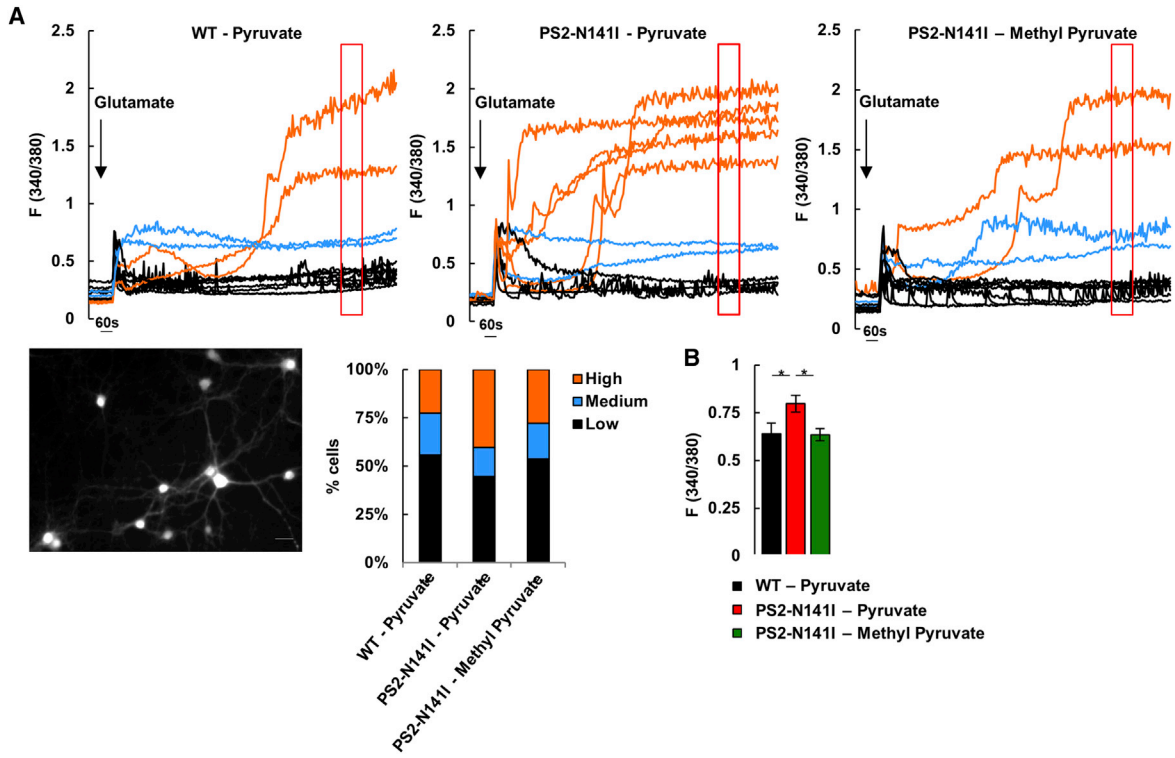

Figure 6. Defective Mitochondrial Bioenergetics in FAD-PS2-N141I Neurons Influences Glutamate-Dependent Neuronal Ca^{2+} Excitotoxicity

(A) Primary cortical neurons (DIV 12–14) from WT and PS2-N141I-tg mice were loaded with Fura-2 (bottom, left; scale bar, 10 μm). On top, representative traces of Ca^{2+} dynamics for the indicated conditions are shown. Where indicated, glutamate (0.5 μM) was added and, 15 min after (red boxes), $[Ca^{2+}]_{cyt}$ recovery was evaluated, grouping cells for their F (340/380) ratio (bottom, middle panel; see STAR Methods).

(B) Bars represent the average F (340/380) Fura-2 ratio for neurons treated as in (A), evaluated 15 min after glutamate exposure (see red boxes in A). n = 100–247 cells, 8–19 coverslips from 3 independent experiments. Mean ± SEM. *p < 0.05.

reported to be critical in AD pathogenesis (Hynd et al., 2004; Wang and Reddy, 2017). Importantly, intracellular ATP is fundamental to cope with glutamate-induced cytosolic Ca^{2+} elevations, sustaining cell Ca^{2+} extrusion (Castilho et al., 1998; Nicholls et al., 1999). To dissect the possible impact of the bioenergetic defects observed in our AD cell models on neuronal activity, we performed Ca^{2+} measurements in cortical neurons from WT and FAD-PS2-N141I-tg mice exposed to glutamate (Figure 6). To evaluate only mitochondrial contribution, glucose was removed and pyruvate was added to the experimental buffer. Compared to WT cells (Figures 6A and 6B, left traces), in face of similar, acute (within seconds) Ca^{2+} rises upon glutamate addition, a higher proportion of FAD-PS2-N141I neurons underwent Ca^{2+} overload after a few minutes (Figures 6A and 6B, middle traces). Importantly, methyl-pyruvate for pyruvate substitution, which recovers OCR in FAD-PS2-expressing cells (Figure 4D), rescued the ability of FAD-PS2-N141I neurons to handle glutamate-induced Ca^{2+} elevations to levels similar to those observed in WT cells (Figures 6A and 6B, right traces).

DISCUSSION

Different alterations in mitochondrial functionality have been consistently reported in AD, but the underlying mechanisms are poorly understood (Ankarcrona et al., 2010; Moreira et al., 2010; Swerdlow et al., 2014).

Here, we found that, in different FAD-PS2-based models, mitochondrial ATP synthesis is impaired. The phenomenon depends on a defective pyruvate oxidation within mitochondria, partly due to a reduced Ca^{2+}-mediated stimulation of the TCA cycle and partly to a dampened mitochondrial pyruvate uptake. Importantly, the defective pyruvate uptake appears as a feature potentially conserved within different AD models. Indeed, we demonstrated that the defect is associated with a reduced recruitment of HK1 to mitochondria, observed not only in our multiple FAD-PS2 models but also after cells exposure to endogenously produced Aβ peptides, i.e., a condition frequently retrieved in AD (Lu et al., 2014). Interestingly, a reduced HK1-mitochondria association has been reported to occur also in PD, DJ1-lacking rodent models and to inhibit the PINK1/Parkin pathway, affecting mitochondrial integrity (Hauser et al., 2017). Importantly, GSK-3β hyper-activation, consistently reported in AD and responsible for *tau* hyperphosphorylation and accumulation into neurofibrillary tangles (Llorens-Martín et al., 2014), is known to induce the detachment of HK1 from mitochondria by phosphorylating VDAC, which binds HK1 to the OMM (Pastorino and Hoek, 2008). Accordingly, our data suggest that GSK-3β inhibition improves mitochondrial ATP production and rescues OCR in FAD-PS2-expressing cells.

The mechanisms leading to GSK-3β hyper-activation in AD are not completely clear. Different studies reported that the cytosolic loop of PSs interacts with GSK-3β, forming a scaffold structure that recruits and activates the enzyme into specific sub-cellular domains (Banerjee et al., 2018; Dolma et al., 2014; Takashima et al., 1998), although also Aβ has been demonstrated to activate GSK-3β, which in turn enhances Aβ production, establishing a pathological feedforward loop (reviewed in Llorens-Martín et al., 2014). Interestingly, a pool of GSK-3β has been shown to reside at contact sites between ER and mitochondria (known as mitochondria-associated membranes [MAMs]; Bantug et al., 2018), where it regulates VDAC phosphorylation and HK1-mitochondria association and thus modulates mitochondrial metabolite flux, TCA cycle, and respiration (Bantug et al., 2018). Intriguingly, both PS1 and PS2 are enriched at MAMs and, in different AD models, MAM upregulation has been consistently reported (Area-Gomez et al., 2012; Hedskog et al., 2013; Kipanyula et al., 2012; Zampese et al., 2011). Moreover, a fraction of Aβ is produced in MAMs (Schreiner et al., 2015), and cell exposure to Aβ alters MAM functionality (Hedskog et al., 2013). This suggests the possibility that, in AD, MAM alterations may converge on a localized GSK-3β activation, inducing HK1 detachment from mitochondria, eventually resulting in defective mitochondrial metabolism (Shoshan-Barmatz and Mizrachi, 2012).

Our FAD-PS2 models show reduced endogenous MPC2 but unaltered MPC1 levels, likely due to a different protein stability when disengaged from the respective molecular partners. Interestingly, GSK-3β inhibition, which recovers mitochondrial ATP synthesis, fully rescues MPC2 expression, further suggesting that the GSK-3β/VDAC/HK1/MPC pathway may be intimately linked to the bioenergetic defects observed in our AD models. Mechanistically, it is possible that HK1, bound to VDAC, forms a complex on the OMM that contacts and/or stabilizes MPCs on specific IMM sub-domains, whereas HK1 detachment might trigger MPC disassembling or mis-targeting, an event that, in the long term, can influence the turnover of specific subunits. Indeed, after 6 h treatment with CMT, we observed reduced MPC2 levels (Figure 4J). Of note, contact sites between OMM and IMM, mediated by specific protein complexes, are emerging as key mitochondrial sub-regions essential for processes such as mitochondrial protein import and metabolite exchange (Aaltonen et al., 2016; Wollweber et al., 2017). Remarkably, VDAC on the OMM is known to form a functional complex with the ATP/ADP translocator (ANT) on the IMM at specific contact sites (Allouche et al., 2012; Vyssokikh and Brdiczka, 2003; Vyssokikh et al., 2001; Brdiczka et al., 2006). A similar mechanism may exist for pyruvate uptake, with the formation of macromolecular complexes (tuned by HK1-mitochondria association) favoring a more direct tunneling of this substrate from the cytosol to the mitochondrial matrix.

As to the impact that mitochondrial pyruvate flux impairment could have on AD onset and/or progression, our data show an increased susceptibility of FAD-PS2-N141I neurons to glutamate-induced excitotoxicity, recovered by feeding mitochondria with methyl-pyruvate. Indeed, evidence has accumulated indicating that, whenever the mitochondrial pathway for pyruvate utilization is impaired, deep changes in brain physiology occur. In mice, loss of MPC1 results in embryonic lethality associated with morphological and functional defects in the brain (Vanderperre et al., 2016). In humans, the rare neurological disorder pyruvate-dehydrogenase-complex-deficiency (PDCD) is caused by a deficiency in one of the components of the PDH complex, the mitochondrial enzyme that converts pyruvate into acetyl-CoA. Interestingly, in PDCD patients, because of its impaired mitochondrial flux, pyruvate accumulates in the cytosol and is massively converted into lactate and alanine, whose increased circulating levels, as well as a switch to the use of alternative mitochondrial substrates, are considered classical biomarkers for diagnosis (Patel et al., 2012; Sofou et al., 2017). Of note, similar, though milder, alterations in the circulating levels of key metabolites linked to mitochondrial activity have been reported in AD (Liguori et al., 2015; Trushina et al., 2013; Wilkins and Trushina, 2018).

Our data, unraveling mitochondrial pyruvate hypo-utilization in AD models, are in line with the well-established AD clinical observation of glucose hypo-metabolism in specific brain regions (Minoshima et al., 1997). Indeed, though our cell models did not display lower cytosolic pyruvate levels or a reduced glycolysis, it is possible that, over years, in the brain of AD patients, the defective mitochondrial pyruvate flux is further worsened by a progressively reduced glucose uptake.

The connection between AD and different metabolic disorders, such as type 2 diabetes, is emerging as a promising, so far poorly explored area of study (Cai et al., 2012; Craft, 2009). Surely, the characterization of specific metabolic fingerprints, associated with AD, would help the better understanding of key pathogenic mechanisms underlying disease onset and progression, opening novel diagnostic and therapeutic opportunities.

STAR★METHODS

Detailed methods are provided in the online version of this paper and include the following:

- KEY RESOURCES TABLE
- LEAD CONTACT AND MATERIALS AVAILABILITY
- EXPERIMENTAL MODEL AND SUBJECT DETAILS
  - Cells
  - Mice
- METHOD DETAILS
  - Transfection and plasmids
  - Primary neuronal cultures
  - Mitochondria isolation
  - Oxygen consumption rate (OCR) in isolated mitochondria
  - Mitochondria membrane potential measurements in isolated mitochondria
  - Mitochondrial ATP hydrolysis in isolated mitochondria
  - Nonyl Acridine Orange (NAO) staining
  - Total cellular ATP measurements
  - Luciferase ATP Measurements
  - FRET experiments
  - Ca^{2+} Measurements: Aequorin
  - Ca^{2+} measurments: Fura-2

- Preparation of protein extracts, Western Blot analysis and ELISA
- Co-immunoprecipitation
- BNE Gel and Sample Preparation
- Oxygen Consumption Rate (OCR) and ECAR measurements in living cells
- Mitochondrial Transmembrane Potential Measurements in living cells
- Immunofluorescence (IF) and confocal analysis
- Drugs
- Antibodies

- QUANTIFICATION AND STATISTICAL ANALYSIS
- DATA AND CODE AVAILABILITY

SUPPLEMENTAL INFORMATION

Supplemental Information can be found online at https://doi.org/10.1016/j.celrep.2020.01.060.

ACKNOWLEDGMENTS

This work was funded by the Italian Ministry of University and Scientific Research (PRIN 2017), the University of Padua (SID 2019), the EU Joint Programme-Neurodegenerative Disease Research (CeBioND), the Cassa di Risparmio di Padova e Rovigo Foundation (CARIPARO Starting Grant 2015) to P.P., and the UNIPD Funds for Research Equipment (2015). The authors would like to thank T. Pozzan for helpful discussions and continuous support; L. Ozmen and F. Hoffmann-La Roche Ltd. (Basel, Switzerland) for kindly donating the transgenic AD mouse model; R. Rizzuto, S. John, B. Ribalet, L.F. Barros, T. Nagai, and J.C. Martinou for sharing plasmids; E. Scremin and C. Fasolato for performing the ELISA assay; and G. Gherardi for helping with the BODIPY assay.

AUTHOR CONTRIBUTIONS

A.R., P.P., and R.F. were responsible for experimental designs, data interpretation, and writing of the paper. G.R. and E.B. designed, performed, and analyzed experiments with isolated mitochondria and hippocampal neurons. G.V. and V.G. designed and performed blue-native gel electrophoresis (BNE) experiments. V.G. performed nonyl acridine orange (NAO) experiments and helped with OCR data interpretation. A.R. and R.F. performed and analyzed all the other experiments. A.R., G.R., G.V., V.G., E.B., P.P., and R.F. discussed the results. P.P. provided funds.

DECLARATION OF INTERESTS

The authors declare no competing interests.

Received: August 19, 2019
Revised: December 4, 2019
Accepted: January 17, 2020
Published: February 18, 2020

REFERENCES

Aaltonen, M.J., Friedman, J.R., Osman, C., Salin, B., di Rago, J.P., Nunnari, J., Langer, T., and Tatsuta, T. (2016). MICOS and phospholipid transfer by Ups2-Mdm35 organize membrane lipid synthesis in mitochondria. J. Cell Biol. *213*, 525–534.

Agostini, M., and Fasolato, C. (2016). When, where and how? Focus on neuronal calcium dysfunctions in Alzheimer's disease. Cell Calcium *60*, 289–298.

Allouche, M., Pertuiset, C., Robert, J.L., Martel, C., Veneziano, R., Henry, C., dein, O.S., Saint, N., Brenner, C., and Chopineau, J. (2012). ANT-VDAC1 interaction is direct and depends on ANT isoform conformation in vitro. Biochem. Biophys. Res. Commun. *429*, 12–17.

Ankarcrona, M., Mangialasche, F., and Winblad, B. (2010). Rethinking Alzheimer's disease therapy: are mitochondria the key? J. Alzheimers Dis. *20* (*Suppl 2*), S579–S590.

Area-Gomez, E., Del Carmen Lara Castillo, M., Tambini, M.D., Guardia-Laguarta, C., de Groof, A.J., Madra, M., Ikenouchi, J., Umeda, M., Bird, T.D., Sturley, S.L., and Schon, E.A. (2012). Upregulated function of mitochondria-associated ER membranes in Alzheimer disease. EMBO J. *31*, 4106–4123.

Banerjee, R., Rudloff, Z., Naylor, C., Yu, M.C., and Gunawardena, S. (2018). The presenilin loop region is essential for glycogen synthase kinase 3 β (GSK3β) mediated functions on motor proteins during axonal transport. Hum. Mol. Genet. *27*, 2986–3001.

Bantug, G.R., Fischer, M., Grählert, J., Balmer, M.L., Unterstab, G., Develioglu, L., Steiner, R., Zhang, L., Costa, A.S.H., Gubser, P.M., et al. (2018). Mitochondria-endoplasmic reticulum contact sites function as immunometabolic hubs that orchestrate the rapid recall response of memory CD8+ T cells. Immunity *48*, 542–555.e6.

Bell, C.J., Bright, N.A., Rutter, G.A., and Griffiths, E.J. (2006). ATP regulation in adult rat cardiomyocytes: time-resolved decoding of rapid mitochondrial calcium spiking imaged with targeted photoproteins. J. Biol. Chem. *281*, 28058–28067.

Bender, T., Pena, G., and Martinou, J.C. (2015). Regulation of mitochondrial pyruvate uptake by alternative pyruvate carrier complexes. EMBO J. *34*, 911–924.

Bhat, R., Xue, Y., Berg, S., Hellberg, S., Ormö, M., Nilsson, Y., Radesäter, A.C., Jerning, E., Markgren, P.O., Borgegård, T., et al. (2003). Structural insights and biological effects of glycogen synthase kinase 3-specific inhibitor AR-A014418. J. Biol. Chem. *278*, 45937–45945.

Brand, M.D., and Nicholls, D.G. (2011). Assessing mitochondrial dysfunction in cells. Biochem. J. *435*, 297–312.

Brdiczka, D.G., Zorov, D.B., and Sheu, S.S. (2006). Mitochondrial contact sites: their role in energy metabolism and apoptosis. Biochim. Biophys. Acta *1762*, 148–163.

Bricker, D.K., Taylor, E.B., Schell, J.C., Orsak, T., Boutron, A., Chen, Y.C., Cox, J.E., Cardon, C.M., Van Vranken, J.G., Dephoure, N., et al. (2012). A mitochondrial pyruvate carrier required for pyruvate uptake in yeast, Drosophila, and humans. Science *337*, 96–100.

Brini, M., Marsault, R., Bastianutto, C., Alvarez, J., Pozzan, T., and Rizzuto, R. (1995). Transfected aequorin in the measurement of cytosolic Ca2+ concentration ([Ca2+]c). A critical evaluation. J. Biol. Chem. *270*, 9896–9903.

Brunello, L., Zampese, E., Florean, C., Pozzan, T., Pizzo, P., and Fasolato, C. (2009). Presenilin-2 dampens intracellular Ca^{2+} stores by increasing Ca^{2+} leakage and reducing Ca^{2+} uptake. J. Cell. Mol. Med. *13* (*9B*), 3358–3369.

Cai, H., Cong, W.N., Ji, S., Rothman, S., Maudsley, S., and Martin, B. (2012). Metabolic dysfunction in Alzheimer's disease and related neurodegenerative disorders. Curr. Alzheimer Res. *9*, 5–17.

Calì, T., Ottolini, D., and Brini, M. (2012). Mitochondrial Ca(2+) and neurodegeneration. Cell Calcium *52*, 73–85.

Cárdenas, C., Miller, R.A., Smith, I., Bui, T., Molgó, J., Müller, M., Vais, H., Cheung, K.H., Yang, J., Parker, I., et al. (2010). Essential regulation of cell bioenergetics by constitutive InsP3 receptor Ca2+ transfer to mitochondria. Cell *142*, 270–283.

Castilho, R.F., Hansson, O., Ward, M.W., Budd, S.L., and Nicholls, D.G. (1998). Mitochondrial control of acute glutamate excitotoxicity in cultured cerebellar granule cells. J. Neurosci. *18*, 10277–10286.

Celsi, F., Pizzo, P., Brini, M., Leo, S., Fotino, C., Pinton, P., and Rizzuto, R. (2009). Mitochondria, calcium and cell death: a deadly triad in neurodegeneration. Biochim. Biophys. Acta *1787*, 335–344.

Chiara, F., Castellaro, D., Marin, O., Petronilli, V., Brusilow, W.S., Juhaszova, M., Sollott, S.J., Forte, M., Bernardi, P., and Rasola, A. (2008). Hexokinase II detachment from mitochondria triggers apoptosis through the permeability

transition pore independent of voltage-dependent anion channels. PLoS ONE *3*, e1852.

Cieri, D., Vicario, M., Giacomello, M., Vallese, F., Filadi, R., Wagner, T., Pozzan, T., Pizzo, P., Scorrano, L., Brini, M., and Calì, T. (2018). SPLICS: a split green fluorescent protein-based contact site sensor for narrow and wide heterotypic organelle juxtaposition. Cell Death Differ. *25*, 1131–1145.

Compan, V., Pierredon, S., Vanderperre, B., Krznar, P., Marchiq, I., Zamboni, N., Pouyssegur, J., and Martinou, J.C. (2015). Monitoring mitochondrial pyruvate carrier activity in real time using a BRET-based biosensor: investigation of the Warburg effect. Mol. Cell *59*, 491–501.

Craft, S. (2009). The role of metabolic disorders in Alzheimer disease and vascular dementia: two roads converged. Arch. Neurol. *66*, 300–305.

Currie, E., Schulze, A., Zechner, R., Walther, T.C., and Farese, R.V., Jr. (2013). Cellular fatty acid metabolism and cancer. Cell Metab. *18*, 153–161.

DeBerardinis, R.J., Lum, J.J., Hatzivassiliou, G., and Thompson, C.B. (2008). The biology of cancer: metabolic reprogramming fuels cell growth and proliferation. Cell Metab. *7*, 11–20.

Del Arco, A., Contreras, L., Pardo, B., and Satrustegui, J. (2016). Calcium regulation of mitochondrial carriers. Biochim. Biophys. Acta *1863*, 2413–2421.

Denton, R.M. (2009). Regulation of mitochondrial dehydrogenases by calcium ions. Biochim. Biophys. Acta *1787*, 1309–1316.

Dolma, K., Iacobucci, G.J., Hong Zheng, K., Shandilya, J., Toska, E., White, J.A., 2nd, Spina, E., and Gunawardena, S. (2014). Presenilin influences glycogen synthase kinase-3 β (GSK-3β) for kinesin-1 and dynein function during axonal transport. Hum. Mol. Genet. *23*, 1121–1133.

Fedeli, C., Filadi, R., Rossi, A., Mammucari, C., and Pizzo, P. (2019). PSEN2 (presenilin 2) mutants linked to familial Alzheimer disease impair autophagy by altering Ca^{2+} homeostasis. Autophagy *15*, 2044–2062.

Federico, A., Cardaioli, E., Da Pozzo, P., Formichi, P., Gallus, G.N., and Radi, E. (2012). Mitochondria, oxidative stress and neurodegeneration. J. Neurol. Sci. *322*, 254–262.

Filadi, R., Greotti, E., Turacchio, G., Luini, A., Pozzan, T., and Pizzo, P. (2016). Presenilin 2 modulates endoplasmic reticulum-mitochondria coupling by tuning the antagonistic effect of mitofusin 2. Cell Rep. *15*, 2226–2238.

Filadi, R., Theurey, P., and Pizzo, P. (2017). The endoplasmic reticulum-mitochondria coupling in health and disease: Molecules, functions and significance. Cell Calcium *62*, 1–15.

Filadi, R., Leal, N.S., Schreiner, B., Rossi, A., Dentoni, G., Pinho, C.M., Wiehager, B., Cieri, D., Cali, T., Pizzo, P., et al. (2018). TOM70 sustains cell bioenergetics by promoting IP3R3-mediated ER to mitochondria Ca2+ transfer. Curr. Biol. *28*, 369–382.e6.

Filippin, L., Magalhães, P.J., Di Benedetto, G., Colella, M., and Pozzan, T. (2003). Stable interactions between mitochondria and endoplasmic reticulum allow rapid accumulation of calcium in a subpopulation of mitochondria. J. Biol. Chem. *278*, 39224–39234.

Fontaine, E., Eriksson, O., Ichas, F., and Bernardi, P. (1998). Regulation of the permeability transition pore in skeletal muscle mitochondria. Modulation By electron flow through the respiratory chain complex i. J. Biol. Chem. *273*, 12662–12668.

Freland, L., and Beaulieu, J.M. (2012). Inhibition of GSK3 by lithium, from single molecules to signaling networks. Front. Mol. Neurosci. *5*, 14.

Frezza, C. (2017). Mitochondrial metabolites: undercover signalling molecules. Interface Focus *7*, 20160100.

Frezza, C., Cipolat, S., and Scorrano, L. (2007). Organelle isolation: functional mitochondria from mouse liver, muscle and cultured fibroblasts. Nat. Protoc. *2*, 287–295.

Galber, C., Valente, G., von Stockum, S., and Giorgio, V. (2019). Purification of functional F-ATP synthase from blue native PAGE. Methods Mol. Biol. *1925*, 233–243.

Garcia, D., and Shaw, R.J. (2017). AMPK: mechanisms of cellular energy sensing and restoration of metabolic balance. Mol. Cell *66*, 789–800.

Giacomello, M., Barbiero, L., Zatti, G., Squitti, R., Binetti, G., Pozzan, T., Fasolato, C., Ghidoni, R., and Pizzo, P. (2005). Reduction of Ca^{2+} stores and capacitative Ca^{2+} entry is associated with the familial Alzheimer's disease presenilin-2 T122R mutation and anticipates the onset of dementia. Neurobiol. Dis. *18*, 638–648.

Giorgio, V., Bisetto, E., Soriano, M.E., Dabbeni-Sala, F., Basso, E., Petronilli, V., Forte, M.A., Bernardi, P., and Lippe, G. (2009). Cyclophilin D modulates mitochondrial F0F1-ATP synthase by interacting with the lateral stalk of the complex. J. Biol. Chem. *284*, 33982–33988.

Giorgio, V., von Stockum, S., Antoniel, M., Fabbro, A., Fogolari, F., Forte, M., Glick, G.D., Petronilli, V., Zoratti, M., Szabó, I., et al. (2013). Dimers of mitochondrial ATP synthase form the permeability transition pore. Proc. Natl. Acad. Sci. USA *110*, 5887–5892.

Gohil, V.M., Sheth, S.A., Nilsson, R., Wojtovich, A.P., Lee, J.H., Perocchi, F., Chen, W., Clish, C.B., Ayata, C., Brookes, P.S., and Mootha, V.K. (2010). Nutrient-sensitized screening for drugs that shift energy metabolism from mitochondrial respiration to glycolysis. Nat. Biotechnol. *28*, 249–255.

Golpich, M., Amini, E., Mohamed, Z., Azman Ali, R., Mohamed Ibrahim, N., and Ahmadiani, A. (2017). Mitochondrial dysfunction and biogenesis in neurodegenerative diseases: pathogenesis and treatment. CNS Neurosci. Ther. *23*, 5–22.

Greotti, E., Wong, A., Pozzan, T., Pendin, D., and Pizzo, P. (2016). Characterization of the ER-targeted low affinity Ca(2+) probe D4ER. Sensors (Basel) *16*, E1419.

Haass, C., and Selkoe, D.J. (2007). Soluble protein oligomers in neurodegeneration: lessons from the Alzheimer's amyloid beta-peptide. Nat. Rev. Mol. Cell Biol. *8*, 101–112.

Hauser, D.N., Mamais, A., Conti, M.M., Primiani, C.T., Kumaran, R., Dillman, A.A., Langston, R.G., Beilina, A., Garcia, J.H., Diaz-Ruiz, A., et al. (2017). Hexokinases link DJ-1 to the PINK1/parkin pathway. Mol. Neurodegener. *12*, 70.

Hedskog, L., Pinho, C.M., Filadi, R., Rönnbäck, A., Hertwig, L., Wiehager, B., Larssen, P., Gellhaar, S., Sandebring, A., Westerlund, M., et al. (2013). Modulation of the endoplasmic reticulum-mitochondria interface in Alzheimer's disease and related models. Proc. Natl. Acad. Sci. USA *110*, 7916–7921.

Herzig, S., Raemy, E., Montessuit, S., Veuthey, J.L., Zamboni, N., Westermann, B., Kunji, E.R., and Martinou, J.C. (2012). Identification and functional expression of the mitochondrial pyruvate carrier. Science *337*, 93–96.

Hynd, M.R., Scott, H.L., and Dodd, P.R. (2004). Glutamate-mediated excitotoxicity and neurodegeneration in Alzheimer's disease. Neurochem. Int. *45*, 583–595.

Imamura, H., Nhat, K.P., Togawa, H., Saito, K., Iino, R., Kato-Yamada, Y., Nagai, T., and Noji, H. (2009). Visualization of ATP levels inside single living cells with fluorescence resonance energy transfer-based genetically encoded indicators. Proc. Natl. Acad. Sci. USA *106*, 15651–15656.

John, S., Weiss, J.N., and Ribalet, B. (2011). Subcellular localization of hexokinases I and II directs the metabolic fate of glucose. PLoS ONE *6*, e17674.

Jouaville, L.S., Pinton, P., Bastianutto, C., Rutter, G.A., and Rizzuto, R. (1999). Regulation of mitochondrial ATP synthesis by calcium: evidence for a long-term metabolic priming. Proc. Natl. Acad. Sci. USA *96*, 13807–13812.

Kipanyula, M.J., Contreras, L., Zampese, E., Lazzari, C., Wong, A.K.C., Pizzo, P., Fasolato, C., and Pozzan, T. (2012). Ca^{2+} dysregulation in neurons from transgenic mice expressing mutant presenilin 2. Aging Cell *11*, 885–893.

Kremer, A., Louis, J.V., Jaworski, T., and Van Leuven, F. (2011). GSK3 and Alzheimer's disease: facts and fiction…. Front. Mol. Neurosci. *4*, 17.

Leroy, K., Yilmaz, Z., and Brion, J.P. (2007). Increased level of active GSK-3beta in Alzheimer's disease and accumulation in argyrophilic grains and in neurones at different stages of neurofibrillary degeneration. Neuropathol. Appl. Neurobiol. *33*, 43–55.

Liguori, C., Stefani, A., Sancesario, G., Sancesario, G.M., Marciani, M.G., and Pierantozzi, M. (2015). CSF lactate levels, τ proteins, cognitive decline: a dynamic relationship in Alzheimer's disease. J. Neurol. Neurosurg. Psychiatry *86*, 655–659.

Lin, M.T., and Beal, M.F. (2006). Mitochondrial dysfunction and oxidative stress in neurodegenerative diseases. Nature *443*, 787–795.

Llorens-Martín, M., Jurado, J., Hernández, F., and Avila, J. (2014). GSK-3β, a pivotal kinase in Alzheimer disease. Front. Mol. Neurosci. *7*, 46.

Llorente-Folch, I., Rueda, C.B., Pardo, B., Szabadkai, G., Duchen, M.R., and Satrustegui, J. (2015). The regulation of neuronal mitochondrial metabolism by calcium. J. Physiol. *593*, 3447–3462.

Lu, T., Aron, L., Zullo, J., Pan, Y., Kim, H., Chen, Y., Yang, T.H., Kim, H.M., Drake, D., Liu, X.S., et al. (2014). REST and stress resistance in ageing and Alzheimer's disease. Nature *507*, 448–454.

Luvisetto, S., Pietrobon, D., and Azzone, G.F. (1987). Uncoupling of oxidative phosphorylation. 1. Protonophoric effects account only partially for uncoupling. Biochemistry *26*, 7332–7338.

Magistretti, P.J., and Allaman, I. (2015). A cellular perspective on brain energy metabolism and functional imaging. Neuron *86*, 883–901.

Minoshima, S., Giordani, B., Berent, S., Frey, K.A., Foster, N.L., and Kuhl, D.E. (1997). Metabolic reduction in the posterior cingulate cortex in very early Alzheimer's disease. Ann. Neurol. *42*, 85–94.

Moreira, P.I., Carvalho, C., Zhu, X., Smith, M.A., and Perry, G. (2010). Mitochondrial dysfunction is a trigger of Alzheimer's disease pathophysiology. Biochim. Biophys. Acta *1802*, 2–10.

Nicholls, D.G., Budd, S.L., Castilho, R.F., and Ward, M.W. (1999). Glutamate excitotoxicity and neuronal energy metabolism. Ann. N Y Acad. Sci. *893*, 1–12.

Olson, K.A., Schell, J.C., and Rutter, J. (2016). Pyruvate and metabolic flexibility: illuminating a path toward selective cancer therapies. Trends Biochem. Sci. *41*, 219–230.

Ovens, M.J., Davies, A.J., Wilson, M.C., Murray, C.M., and Halestrap, A.P. (2010). AR-C155858 is a potent inhibitor of monocarboxylate transporters MCT1 and MCT2 that binds to an intracellular site involving transmembrane helices 7-10. Biochem. J. *425*, 523–530.

Ozmen, L., Albientz, A., Czech, C., and Jacobsen, H. (2009). Expression of transgenic APP mRNA is the key determinant for beta-amyloid deposition in PS2APP transgenic mice. Neurodegener. Dis. *6*, 29–36.

Palmer, A.E., and Tsien, R.Y. (2006). Measuring calcium signaling using genetically targetable fluorescent indicators. Nat. Protoc. *1*, 1057–1065.

Pastorino, J.G., and Hoek, J.B. (2008). Regulation of hexokinase binding to VDAC. J. Bioenerg. Biomembr. *40*, 171–182.

Pastorino, J.G., Hoek, J.B., and Shulga, N. (2005). Activation of glycogen synthase kinase 3beta disrupts the binding of hexokinase II to mitochondria by phosphorylating voltage-dependent anion channel and potentiates chemotherapy-induced cytotoxicity. Cancer Res. *65*, 10545–10554.

Patel, K.P., O'Brien, T.W., Subramony, S.H., Shuster, J., and Stacpoole, P.W. (2012). The spectrum of pyruvate dehydrogenase complex deficiency: clinical, biochemical and genetic features in 371 patients. Mol. Genet. Metab. *105*, 34–43.

Pathak, D., Shields, L.Y., Mendelsohn, B.A., Haddad, D., Lin, W., Gerencser, A.A., Kim, H., Brand, M.D., Edwards, R.H., and Nakamura, K. (2015). The role of mitochondrially derived ATP in synaptic vesicle recycling. J. Biol. Chem. *290*, 22325–22336.

Patron, M., Checchetto, V., Raffaello, A., Teardo, E., Vecellio Reane, D., Mantoan, M., Granatiero, V., Szabò, I., De Stefani, D., and Rizzuto, R. (2014). MICU1 and MICU2 finely tune the mitochondrial Ca^{2+} uniporter by exerting opposite effects on MCU activity. Mol. Cell *53*, 726–737.

Pinton, P., and Rizzuto, R. (2006). Bcl-2 and Ca^{2+} homeostasis in the endoplasmic reticulum. Cell Death Differ. *13*, 1409–1418.

Qin, W., Peng, Y., Ksiezak-Reding, H., Ho, L., Stetka, B., Lovati, E., and Pasinetti, G.M. (2006). Inhibition of cyclooxygenase as potential novel therapeutic strategy in N141I presenilin-2 familial Alzheimer's disease. Mol. Psychiatry *11*, 172–181.

Rambold, A.S., Cohen, S., and Lippincott-Schwartz, J. (2015). Fatty acid trafficking in starved cells: regulation by lipid droplet lipolysis, autophagy, and mitochondrial fusion dynamics. Dev. Cell *32*, 678–692.

Rangaraju, V., Calloway, N., and Ryan, T.A. (2014). Activity-driven local ATP synthesis is required for synaptic function. Cell *156*, 825–835.

Rizzuto, R., Simpson, A.W., Brini, M., and Pozzan, T. (1992). Rapid changes of mitochondrial Ca^{2+} revealed by specifically targeted recombinant aequorin. Nature *358*, 325–327.

Robey, R.B., and Hay, N. (2006). Mitochondrial hexokinases, novel mediators of the antiapoptotic effects of growth factors and Akt. Oncogene *25*, 4683–4696.

Rossi, A., Pizzo, P., and Filadi, R. (2019). Calcium, mitochondria and cell metabolism: A functional triangle in bioenergetics. Biochim Biophys Acta Mol Cell Res *1866*, 1068–1078.

San Martín, A., Ceballo, S., Baeza-Lehnert, F., Lerchundi, R., Valdebenito, R., Contreras-Baeza, Y., Alegría, K., and Barros, L.F. (2014). Imaging mitochondrial flux in single cells with a FRET sensor for pyruvate. PLoS ONE *9*, e85780.

Schon, E.A., and Manfredi, G. (2003). Neuronal degeneration and mitochondrial dysfunction. J. Clin. Invest. *111*, 303–312.

Schreiner, B., Hedskog, L., Wiehager, B., and Ankarcrona, M. (2015). Amyloid-β peptides are generated in mitochondria-associated endoplasmic reticulum membranes. J. Alzheimers Dis. *43*, 369–374.

Shoshan-Barmatz, V., and Mizrachi, D. (2012). VDAC1: from structure to cancer therapy. Front. Oncol. *2*, 164.

Shoshan-Barmatz, V., Krelin, Y., and Shteinfer-Kuzmine, A. (2018). VDAC1 functions in Ca^{2+} homeostasis and cell life and death in health and disease. Cell Calcium *69*, 81–100.

Sofou, K., Dahlin, M., Hallböök, T., Lindefeldt, M., Viggedal, G., and Darin, N. (2017). Ketogenic diet in pyruvate dehydrogenase complex deficiency: short- and long-term outcomes. J. Inherit. Metab. Dis. *40*, 237–245.

Sun, L., Shukair, S., Naik, T.J., Moazed, F., and Ardehali, H. (2008). Glucose phosphorylation and mitochondrial binding are required for the protective effects of hexokinases I and II. Mol. Cell. Biol. *28*, 1007–1017.

Swerdlow, R.H., Burns, J.M., and Khan, S.M. (2014). The Alzheimer's disease mitochondrial cascade hypothesis: progress and perspectives. Biochim. Biophys. Acta *1842*, 1219–1231.

Takanaga, H., Chaudhuri, B., and Frommer, W.B. (2008). GLUT1 and GLUT9 as major contributors to glucose influx in HepG2 cells identified by a high sensitivity intramolecular FRET glucose sensor. Biochim. Biophys. Acta *1778*, 1091–1099.

Takashima, A., Murayama, M., Murayama, O., Kohno, T., Honda, T., Yasutake, K., Nihonmatsu, N., Mercken, M., Yamaguchi, H., Sugihara, S., and Wolozin, B. (1998). Presenilin 1 associates with glycogen synthase kinase-3beta and its substrate tau. Proc. Natl. Acad. Sci. USA *95*, 9637–9641.

Taylor, E.B. (2017). Functional properties of the mitochondrial carrier system. Trends Cell Biol. *27*, 633–644.

Theurey, P., Connolly, N.M.C., Fortunati, I., Basso, E., Lauwen, S., Ferrante, C., Moreira Pinho, C., Joselin, A., Gioran, A., Bano, D., et al. (2019). Systems biology identifies preserved integrity but impaired metabolism of mitochondria due to a glycolytic defect in Alzheimer's disease neurons. Aging Cell *18*, e12924.

Trushina, E., Dutta, T., Persson, X.M., Mielke, M.M., and Petersen, R.C. (2013). Identification of altered metabolic pathways in plasma and CSF in mild cognitive impairment and Alzheimer's disease using metabolomics. PLoS ONE *8*, e63644.

Vacanti, N.M., Divakaruni, A.S., Green, C.R., Parker, S.J., Henry, R.R., Ciaraldi, T.P., Murphy, A.N., and Metallo, C.M. (2014). Regulation of substrate utilization by the mitochondrial pyruvate carrier. Mol. Cell *56*, 425–435.

Vanderperre, B., Herzig, S., Krznar, P., Hörl, M., Ammar, Z., Montessuit, S., Pierredon, S., Zamboni, N., and Martinou, J.C. (2016). Embryonic lethality of mitochondrial pyruvate carrier 1 deficient mouse can be rescued by a ketogenic diet. PLoS Genet. *12*, e1006056.

Vyssokikh, M.Y., and Brdiczka, D. (2003). The function of complexes between the outer mitochondrial membrane pore (VDAC) and the adenine nucleotide translocase in regulation of energy metabolism and apoptosis. Acta Biochim. Pol. *50*, 389–404.

Vyssokikh, M.Y., Katz, A., Rueck, A., Wuensch, C., Dörner, A., Zorov, D.B., and Brdiczka, D. (2001). Adenine nucleotide translocator isoforms 1 and 2 are differently distributed in the mitochondrial inner membrane and have distinct affinities to cyclophilin D. Biochem. J. *358*, 349–358.

Wang, R., and Reddy, P.H. (2017). Role of glutamate and NMDA receptors in Alzheimer's disease. J. Alzheimers Dis. *57*, 1041–1048.

Wiederkehr, A., Szanda, G., Akhmedov, D., Mataki, C., Heizmann, C.W., Schoonjans, K., Pozzan, T., Spät, A., and Wollheim, C.B. (2011). Mitochondrial matrix calcium is an activating signal for hormone secretion. Cell Metab. *13*, 601–611.

Wilkins, J.M., and Trushina, E. (2018). Application of metabolomics in Alzheimer's disease. Front. Neurol. *8*, 719.

Wollweber, F., von der Malsburg, K., and van der Laan, M. (2017). Mitochondrial contact site and cristae organizing system: A central player in membrane shaping and crosstalk. Biochim Biophys Acta Mol Cell Res *1864*, 1481–1489.

Yang, C., Ko, B., Hensley, C.T., Jiang, L., Wasti, A.T., Kim, J., Sudderth, J., Calvaruso, M.A., Lumata, L., Mitsche, M., et al. (2014). Glutamine oxidation maintains the TCA cycle and cell survival during impaired mitochondrial pyruvate transport. Mol. Cell *56*, 414–424.

Zal, T., and Gascoigne, N.R. (2004). Photobleaching-corrected FRET efficiency imaging of live cells. Biophys. J. *86*, 3923–3939.

Zampese, E., and Pizzo, P. (2012). Intracellular organelles in the saga of Ca2+ homeostasis: different molecules for different purposes? Cell. Mol. Life Sci. *69*, 1077–1104.

Zampese, E., Fasolato, C., Kipanyula, M.J., Bortolozzi, M., Pozzan, T., and Pizzo, P. (2011). Presenilin 2 modulates endoplasmic reticulum (ER)-mitochondria interactions and Ca^{2+} cross-talk. Proc. Natl. Acad. Sci. USA *108*, 2777–2782.

Zatti, G., Ghidoni, R., Barbiero, L., Binetti, G., Pozzan, T., Fasolato, C., and Pizzo, P. (2004). The presenilin 2 M239I mutation associated with familial Alzheimer's disease reduces Ca^{2+} release from intracellular stores. Neurobiol. Dis. *15*, 269–278.

Zatti, G., Burgo, A., Giacomello, M., Barbiero, L., Ghidoni, R., Sinigaglia, G., Florean, C., Bagnoli, S., Binetti, G., Sorbi, S., et al. (2006). Presenilin mutations linked to familial Alzheimer's disease reduce endoplasmic reticulum and Golgi apparatus calcium levels. Cell Calcium *39*, 539–550.

STAR★METHODS

KEY RESOURCES TABLE

REAGENT or RESOURCE	SOURCE	IDENTIFIER
Antibodies		
Mouse monoclonal anti-actin (AC-40)	Sigma-Aldrich	Cat#A4700; RRID:AB_476730
Rabbit polyclonal anti-AMPK	Cell Signaling	Cat#2532S; RRID:AB_330331
Rabbit polyclonal anti-Phospho-AMPK(Thr172)	Cell Signaling	Cat#2531S; RRID:AB_330330
Mouse monoclonal anti-cytochrome *c*	Cell Signaling	Cat#12963; RRID:AB_2637072
Rabbit monoclonal anti-GSK3 α/β	Cell Signaling	Cat#5676; RRID:AB_2637072
Rabbit polyclonal anti-phospho Y216/Y279 GSK3 α/β	Abcam,	Cat#ab4797; RRID:AB_304634
Mouse monoclonal anti-FLAG(M2)	Sigma Aldrich	Cat#F3165; RRID:AB_259529
Rabbit monoclonal anti-FLAG	Sigma Aldrich	Cat#F7425; RRID:AB_439687
Mouse monoclonal anti-MYC	Sigma Aldrich	Cat#05-724; RRID:AB_309938
Rabbit monoclonal anti-MYC	Cell Signaling	Cat#2278; RRID:AB_490778
Rabbit monoclonal anti-HK1	Thermo Scientific Pierce	Cat#MA5-14789; RRID:AB_10987238
Rabbit monoclonal anti-MPC1	Cell Signaling,	Cat#D2L9I-14462; RRID:AB_2773729
Rabbit monoclonal anti-MPC2	Cell Signaling,	Cat#D4I7G-46141; RRID:AB_2799295
Rabbit anti-OXPHOS, MitoProfile	MitoSciences	Cat#MS604; RRID:AB_2629281
Mouse monoclonal anti-tubulin (10D8)	Santa Cruz Biotech	Cat#sc-53646; RRID:AB_630403
Mouse monoclonal anti-TIM23	BD Biosciences	Cat#611222; RRID:AB_398754
Rabbit anti-phospho-PDH	Millipore	Cat#ABS204; RRID:AB_11205754
Mouse anti-PDH	Santa Cruz Biotech	Cat# sc-377092; RRID:AB_2716767
Chemicals, Peptides, and Recombinant Proteins		
Ciclopiazonic acid (CPA,);	Abcam biochemical	ab120300
Gramicidin-A	Abcam	ab144510
UK-5099	Sigma Aldrich	PZ0160
Pioglitazone hydrochloride	Sigma Aldrich	E6910
oligomycin-A	Sigma Aldrich	75351
carbonyl cyanide-4-(trifluoromethoxy) phenylhydrazone (FCCP)	Sigma Aldrich	C2920
Clotrimazole	Sigma Aldrich	C6019
rotenone	Sigma Aldrich	R8875
antimycin-A	Sigma Aldrich	A8674
AR-C155858	Tocris bioscience	4960
AR-A014418	Sigma Aldrich	A3230
Methyl-Pyruvate	Sigma Aldrich	371173
Etomoxir	Sigma Aldrich	E1905
BPTES	SigmaAldrich	SML0601
Digitonin	Calbiochem	300410
MG132	Sigma Aldrich	M8699
Fura-2 AM	Thermo Fisher Scientific	F1221
Rhodamine 123	Sigma Aldrich	R8004
cycloheximide	Sigma Aldrich	C7698
MG132	Sigma Aldrich	474787
Ouabain	Sigma Aldrich	O3125
BODIPY 558/568 C12	Thermo Fisher Scientific	D3835

(*Continued on next page*)

Continued

REAGENT or RESOURCE	SOURCE	IDENTIFIER
Critical Commercial Assays		
Luciferin/luciferase assay ATPlite 1 step	PerkinElmer	Cat# 6016736
Pierce BCA Protein Assay Kit	Thermo Fisher	Cat# 23225
Experimental Models: Cell Lines		
SH-SY5Y	ATCC	CRL-2266
HT22	Sigma Aldrich	SCC129
MEF	ATCC	CRL-2991
Human fibroblasts FAD-PS2-N141I	Coriell Institute for medical research	AG09908
Human fibroblasts (CTRL1)	Coriell Institute for medical research	AG08525
Human fibroblasts (CTRL2)	Coriell Institute for medical research	AG08269
Human fibroblasts (CTRL3)	Coriell Institute for medical research	AG09173
Experimental Models: Organisms/Strains		
Wild-type mouse: C57BL6/J	The Jackson Laboratory (Jax)	Cat# 000664
Transgenic mouse: PS2.30H	Dr. L Ozmen (F.Hoffmann-La Roche Ltd, Basel, Switzerland	Ozmen et al., 2009; Kipanyula et al., 2012
Oligonucleotides		
Primer FL-HK1-For (5′3′): CGCGGTACCGCCACCATGATCGCCG CGC	This paper	N/A
Primer FL-HK1-Rev (5′3′): GAGCGGC CGCGGCGATCGAAGGGT	This paper	N/A
Primer ΔN-HK1-For (5′3′): CGCGGTA CCGCCACCATGAAGATTGACA AGTATCTGTACGC	This paper	N/A
Primer ΔN-HK1-Rev (5′3′): GAGCGGCCGC GGCGATCGAAGGGT	This paper	N/A
Primer TdTomato-For (5′3′): TTGCGGC CGCCGTGAGCAAGGGCGAGGAG	This paper	N/A
Primer TdTomato-Rev (5′3′): CCGCTC GAGTTACTTGTACAGCTCGTCCATGCC	This paper	N/A
Primer N-Term-TdTomato-For (5′3′): ACGGGATCCGC CACCATGATCGCCGCGCAGCTCCTGGCCTATTA CTTCACGGAGCTGGTGAGCAAGGGCGAGGAG	This paper	N/A
Primer N-Term-TdTomato-Rev (5′3′): CCGC TCGAGTTACTTGTACAGCTCGTCCATGCC	This paper	N/A
Primer MPC1-For (5′3′): GCGGATATCA AGCTTGCCACCATGG	This paper	N/A
See Table S2 for additional nucleotides		N/A
Recombinant DNA		N/A
Matrix-Pyronic	This paper	N/A
MCU-FLAG	Patron et al., 2014	N/A
MICU1EFmut	Patron et al., 2014	N/A
MIMS-Pyronic	This paper	N/A
Mitochondrial-Aequorin	Cai et al., 2012	N/A
Mitochondrial-Ateam1.03	Imamura et al., 2009	N/A
Mitochondrial Cerulean	Filadi et al., 2018	N/A
Mitochondrial Luciferase	Jouaville et al., 1999	N/A
Mitochondrial RFP	Pinton and Rizzuto, 2006	N/A
MPC1-CFP	This paper	N/A
MPC2-YFP	This paper	N/A

(*Continued on next page*)

Continued

REAGENT or RESOURCE	SOURCE	IDENTIFIER
Nuclear-Ateam1.03	Imamura et al., 2009	N/A
PS2WT	Zampese et al., 2011	N/A
PS2-T122R	Zampese et al., 2011	N/A
PS2-N141I	Brunello et al., 2009	N/A
Pyronic	San Martín et al., 2014	N/A
FL-HK1	This paper	N/A
ΔN-HK1	This paper	N/A
mtCFP	Filadi et al., 2018	N/A
ER-β11	Cieri et al., 2018	N/A
FLII12Pglu-700uDelta6	Takanaga et al., 2008	N/A
Software and Algorithms		
ImageJ	National Institutes of Health, Bethesda, MD, USA	https://imagej.nih.gov/ij/download.html
Origin8	OriginLab Corporation	N/A

LEAD CONTACT AND MATERIALS AVAILABILITY

Further information and requests for resources and reagents should be directed to and will be fulfilled by the Lead Contact, Paola Pizzo (paola.pizzo@unipd.it). All unique/stable reagents generated in this study are available from the Lead Contact with a completed Materials Transfer Agreement.

EXPERIMENTAL MODEL AND SUBJECT DETAILS

Cells

SH-SY5Y, HT22 and MEFs cells were grown in DMEM (DMEM 5671, Sigma), supplemented with 10% FCS, L-glutamine (2 mM), penicillin (100 μg/ml) and streptomycin (100 μg/ml). Human fibroblasts from Coriell Institute for medical research (FAD-PS2-N141I (AG09908) and control fibroblasts (AG08525, AG08269, AG09173)) were grown in the same medium, but containing 15% FCS. Cells were grown in a humidified atmosphere containing 5% CO_2 and seeded onto glass coverslips (13, 18 or 24 mm diameter). Where indicated, galactose-containing medium was used: DMEM no glucose (GIBCO, 11966025), supplemented with 10 mM galactose, 5% FCS, L-glutamine (2 mM), penicillin (100 U/ml) and streptomycin (100 μg/ml).

Mice

The transgenic mouse line PS2.30H was used (kindly provided by Dr. L. Ozmen (F. Hoffmann-La Roche Ltd, Basel, Switzerland, see also below. The line has the background strain of C57BL/6 mice, which were used as wt controls (Charles River). Mouse line features:

(1) The PS2.30H is a homozygous single transgenic line expressing the FAD-linked mutant human PS2-N141I under the mouse prion protein promoter. These mice display ~2-fold increase of PS2 levels, both in cortices and hippocampi, compared to wt (Kipanyula et al., 2012).
(2) The C57BL/6J WT mice share > 90% genetic background of the other line.

For primary neuronal cultures, new-born mice (0-P1), mixed for sex, were used. For mitochondria isolation and protein extraction, females at 6 months of age were sacrificed.

METHOD DETAILS

Transfection and plasmids

Transfections were performed at 60% confluence using Lipofectamine 2000 Transfection Reagent (Life Technologies). Cells were transfected with 1.5 μg of DNA in 24 wells/plate (0.5 μg of either Aequorin or luciferase probes together with 1 μg of either pcDNA3 or PS2-T122R or MICU1EFmut or HK1 encoding cDNAs), or with 2 μg of DNA in 12 wells/plate (0.5 μg of Pyronic or ATeam1.03, or 0.3 μg of both MPC1-CFP and MPC2-YFP, together with 1.4 μg of either pcDNA3 or PS2 WT or PS2-T122R or PS2-N141I encoding cDNAs). Seahorse, aequorin, luciferase and FRET measurements were usually performed 24 or 48 h after transfection.

For RNAi experiments, Control siRNA (universal negative control, SIC001, Sigma-Aldrich) and HK1-specific siRNA (mouse HK1, SASI_Mm01_00022875; human HK1, SASI_Hs01_00226390; Sigma-Aldrich), were added to the trasfection mix to a final concentration of 50 nM.

Most of the cDNAs that have been used were previously described: PS2 WT, PS2-T122R and PS2-N141I (Brunello et al., 2009; Zampese et al., 2011); mitochondrial aequorin (Pinton and Rizzuto, 2006); nuclear and mitochondrial Ateam1.03 (Imamura et al., 2009); mitochondrial luciferase (Jouaville et al., 1999); MICU1EFmut and MCU-FLAG (Patron et al., 2014); Pyronic (San Martín et al., 2014); mitochondrial Cerulean and RFP (Filadi et al., 2018; Filippin et al., 2003); ER-β11 (Cieri et al., 2018).

To generate MIMS- and mitochondrial matrix-Pyronic, the sequence encoding mseCFP and the pyruvate-binding domain of the original Pyronic, excluding the DNA-binding motif of PdhR (i.e., excluding the sequence encoding amino acids 1-56, UniProt P0ACL9, that we observed to be toxic when targeted to mitochondria) were synthesized in frame (Life Technologies), flanked by BamHI and EcoRI restriction sites. After enzymatic digestion (BamHI and EcoRI), this sequence was then ligated in frame at the 5′ of that encoding CpV (flanked by EcoRI and XhoI restriction sites) and inserted into pcDNA3 (Life Technologies). The plasmid was then used to generate MIMS- and mitochondrial matrix-targeted Pyronic, as detailed below.

To generate MIMS-Pyronic, the MIMS-targeting sequence was obtained amplifying by PCR the sequence encoding the first 67 amino acids of mouse MICU1, with the following primers:

For (5′3’): CGCAAGCTTATGTTTCGTCTTAACACCCTTT
Rev (5′3’): GCGGGATCCCTTCTTGCTGTTAACGCATG

After enzymatic digestion of the PCR product and of the plasmid described above (HindIII and BamHI), ligation was performed to obtain the plasmid encoding MIMS-Pyronic.

To generate the mitochondrial matrix-targeted Pyronic, the matrix-targeting sequence (4mt, 4x the N-terminal 36 amino acids of the human cytochrome *c* oxidase subunit VIII (Rizzuto et al., 1992)) was obtained by gene synthesis (Life Technologies), flanked by HindIII and BamHI restriction sites. After enzymatic digestion of this sequence and of the plasmid described above, ligation was performed to obtain the mitochondrial matrix-targeted Pyronic.

To generate FL-HK1 and ΔN-HK1 fused with dtTomato, the sequence encoding rat-HK1 (John et al., 2011) was amplified by PCR with the following primers:

FL-HK1
For (5′3’): CGCGGTACCGCCACCATGATCGCCGCGC
Rev (5′3’): GAGCGGCCGCGGCGATCGAAGGGT
ΔN-HK1
For (5′3’): CGCGGTACCGCCACCATGAAGATTGACAAGTATCTGTACGC
Rev (5′3’): GAGCGGCCGCGGCGATCGAAGGGT

tdTomato sequence (tdTomato-C1 was a gift from Michael Davidson, Addgene plasmid # 54653) was amplified by PCR with the following primers:

For (5′3’): TTGCGGCCGCCGTGAGCAAGGGCGAGGAG
Rev (5′3’): CCGCTCGAGTTACTTGTACAGCTCGTCCATGCC

After enzymatic digestion of FL-HK1 and ΔN-HK1 (KpnI and NotI), and of tdTomato (NotI and XhoI), the sequences were inserted into pcDNA3.

Nterm-HK1-tdTomato was generated by PCR with the following primers:

For (5′3’):
ACGGGATCCGCCACCATGATCGCCGCGCAGCTCCTGGCCTATTACTTCACGGAGCTGGTGAGCAAGGGCGAGGAG
Rev (5′3’): CCGCTCGAGTTACTTGTACAGCTCGTCCATGCC

The PCR product was digested (NotI and XhoI) and inserted into pcDNA3.

MPC1-CFP (mCER3 sequence was used instead of CFP) and MPC2 (without the stop codon) sequences were generated by gene synthesis (Life Technologies). After enzymatic digestion (HindIII and BamHI), the sequence of MPC1-CFP was directly inserted into pcDNA3, while that of MPC2 was inserted in frame at the 5′ of CpV sequence (previously inserted between the BamHI and XhoI restriction sites of pcDNA3). MPC1-FLAG and MPC2-MYC sequences were generated by PCR (using MPC1-CFP and MPC2-YFP as templates), with the following primers:

MPC1-For (5′3’): GCGGATATCAAGCTTGCCACCATGG
MPC1-Rev (5′3’):
GCGGGATCCTTACTTGTCGTCATCGTCTTTGTAGTCTGCAGATGCCGTTTTAGTC

MPC2-For (5′3’): AGACCCGGGAAGCTTATGTCGGCCGCC
MPC2-Rev (5′3’):
GCGGGATCCTTACAGGTCTTCTTCAGAGATCAGTTTCTGTTCTTTGTGTGCTTTAGCTTTTAGTTC

After enzymatic digestion (HindIII and BamHI), the PCR products were inserted into pcDNA3.

Primary neuronal cultures

Primary neuronal cultures were obtained from cortices or hippocampi, dissected from 0 to 1 day new-born mice as previously described (Kipanyula et al., 2012). Transgenic mouse line PS2.30H was used (kindly provided by Dr. L. Ozmen (F. Hoffmann-La Roche Ltd, Basel, Switzerland) (Ozmen et al., 2009). The line has the background strain of C57BL/6 mice, which were used as wt controls (Charles River). All procedures were carried out in strict adherence to the Italian regulations on animal protection and care with the explicit approval of the local veterinary authority (Project code: D2784.N.J7L).

Cells were seeded on coated coverslips (poly-L-lysine, 100 μg/mL for cortical; poly-L-lysine 30 μg/ml and laminin 2 μg/ml for hippocampal neurons; 3x105 cells/well, for co-localization experiments, 8x105 cells/well for FRET and Fura-2 experiments) in MEM (GIBCO, 32360026) containing glucose (20 mM), L-glutamine (0.5 mM), B27 supplement (0.5%), N2 supplement (1%), pyruvic acid (1 mM), biotin (3.6 μM), penicillin (25 μg/mL), streptomycin (25 μg/mL), neomycin (50 μg/mL) and horse serum (10%). 24 h after plating, medium was replaced with serum- and antibiotic-free Neurobasal (GIBCO, 10888022) medium (for co-localization experiments) containing B27 (2%) and L-glutamine (0.5 mM), or with BME (GIBCO, 41010026) supplemented with B27 (2%), L-glutamine (0.5 mM) and Sodium Pyruvate (0.23 mM). Fresh medium was added (1/5 of total volume) every 4 days.

Co-localization, western blot and Fura-2 experiments were performed at 10-12 days *in vitro* (DIV); for FRET ATP measurements, the neurons were transfected with Lipofectamine 2000 at 5-6 DIV with 1.2 μg of DNA (0.6 μg H2B ATeam1.03 + 0.6 μg 4mtATeam1.03) and the experiments were performed 24h after transfection.

Mitochondria isolation

Brain

Animals at 6 months of age were sacrificed by cervical dislocation, the procedures were performed by authorized personnel of the animal care facility. Brains were excised from the skulls, and the cortices were separated from olfactory bulbs, cerebellum and brainstem. The cortices were then rapidly transferred in an ice-cold solution (225 mM mannitol, 50 mM sucrose, 10 mM HEPES, 1 mM Pi, 1 mM $MgCl_2$, 1 mM EGTA, 0.2% fatty-acid-free bovine serum albumin and 2 μM Tpen (pH: 7.4)) (dissection medium 1), minced with scissors, and homogenized with few strokes in a glass potter. The homogenate was centrifuged at 2000 g for 3-minutes. The resulting supernatant was centrifuged at 12000 g for 6-minutes; the pellet obtained was resuspended with a large volume of the dissection medium with EGTA 20 μM and without BSA (dissection medium 2) and centrifuged as above. The resulting pellet was resuspended with a low volume of dissection medium 2, and the amount of protein obtained was quantified using the bicinchoninic acid assay (Euroclone). For all the experiments performed with isolated mitochondria, a basic isosmotic saline was used (in mM: 120 KCl, 10 NaCl, 20 HEPES, 1 Pi, and 1 $MgCl_2$).

Cells

Mitochondria from cells were isolated after cell disruption with a glass-Teflon potter in a buffer composed of 250 mM sucrose, 10 mM Tris-HCl, 0.1 mM EGTA-Tris, pH 7.4 as previously described (Frezza et al., 2007). Mitochondria were then used for blue-native electrophoresis.

Oxygen consumption rate (OCR) in isolated mitochondria

Mitochondrial OCR was evaluated polarographically at 25°C using a Clark-type electrode. The experiments were performed with 5 mM succinate as respiratory substrate, 100 μM ADP to measure the ADP-dependent OCR (state 3), 2 μg/ml oligomycin to establish the state 4 and 100 nM FCCP to achieve the uncoupled respiration.

Mitochondria membrane potential measurements in isolated mitochondria

Kinetic, fluorimetric measurements of the mitochondria membrane potential were carried out at 25°C with a Perkin-Elmer 650-40 spectrofluorimeter equipped with magnetic stirring and thermostatic control (Fontaine et al., 1998; Giorgio et al., 2013). Membrane potential was evaluated using 100 nM Rhodamine 123 (λ excitation-emission, 503-527 nm, respectively). During the experiments, upon mitochondria addition (0.5 mg/ml), 5 mM succinate and 4 μM FCCP were sequentially added, and the fluorescence reached at equilibrium after each addition was registered. The observed fluorescence variations can be translated into membrane potential values using the Nernst equilibrium potential equation $\Delta\Psi = 2.3\ RT/nF\ \ln [Xn+]out/[Xn+]in$ where R is the universal gas constant, T the temperature in Kelvin, n the valence of the ion and F is the Faraday’s constant. To adapt the equation to the usage of Rho 123, some assumptions have to be made. First, the non-specific binding of Rhodamine 123 to the mitochondria does not depend on the membrane potential and the resultant fluorescence value is assumed to correspond to 0 mV membrane potential. Second, the fluorescence of the Rho 123 accumulated in the mitochondrial matrix is negligible when compared with the fluorescence of Rho 123 in the medium. And third, Rho 123 fluorescence varies linearly with the cation concentration. With the appropriate substitutions the following equation can be derived $\Delta\Psi = 59.2\ \log10\ [(\Delta F/F)\ x\ (Vext/Vint)]$ where ΔF is the difference between the fluorescence in

the presence of FCCP, F0 (0 mV membrane potential) and the fluorescence of the energized mitochondria F. Assuming that the mitochondrial matrix volume is 1 μL per mg of protein (Vint), and performing the experiments with 0.5 mg/ml of mitochondria in 2 mL total volume (Vext) the equation becomes $\Delta\Psi$ = 59.2 log10 [(ΔF/F) x 2000].The validity of the above equation was verified through comparison with membrane potential values measured with the methyltriphenyl phosphonium ion (TPMP+) electrode (Petronilli V. and Fontaine E., personal communication).

Mitochondrial ATP hydrolysis in isolated mitochondria

This assay is based on the reaction in which the hydrolysis of ATP is coupled to the oxidation of NADH, as previously described (Luvisetto et al., 1987). The experiments were carried out with 0.5 mg/ml of isolated mouse brain mitochondria, suspended in a saline containing 120 mM KCl, 10 mM NaCl, 20 mM HEPES, 1 mM Pi, 1 mM $MgCl_2$, 4 mM phospoenolpyruvate (PEP), 4 U/ml pyruvate kinase, 3 U/ml LDH (lactic dehydrogenase), 0.2 mM NADH and 2 mM ATP. Furthermore, 10 μM ouabain octahydrate and vanadate were added to respectively inhibit the Na^+/K^+ ATPase and some plasma membrane ATPases (such as Na^+/K^+ ATPase and Ca^{2+} ATPase). The measurements were performed with a Cary Series UV-Vis spectrophotometer and the absorbance measured at 340 nm. The rate of NADH oxidation was measured and converted into NADH concentration using the NADH extinction coefficient ε = 6220 M^{-1}, cm^{-1}. Hydrolyzed ATP concentration was obtained knowing that 1 mol of ATP is hydrolyzed for every mol of NADH oxidized. After measurement of basal ATP hydrolysis, resveratrol (200 μM; Sigma Aldrich, R5010) was added to inhibit ATP synthase. The effect of oligomycin (2 μg/ml) addition was also tested and the inhibitory effect was similar in the two genotypes. ATPase activity was calculated by subtracting the rate of ATP hydrolysis after resveratrol addition to the basal rate.

Nonyl Acridine Orange (NAO) staining

NAO staining has been used to measure mitochondrial content in cells. The dye binds specifically cardiolipin in mitochondria. Cells were seeded in a 12 well-plate and transfected as detailed above. NAO dye (200 nM, Sigma) was added to cells 24 h after transfection in mKRB (in mM: 135 NaCl, 5 KCl, 0.4 KH_2PO_4, 1 $MgCl_2$, 1 $CaCl_2$, 20 HEPES, 10 galactose; pH 7.4 at 37°C), in the absence or presence of UK5099, etomoxir or BPTES, at the indicated concentrations. Cells were stained for 30 min at 37°C, washed with mKRB, detached with trypsin, centrifuged at 1,000 x g for 5 min, and suspended in the mKRB at the concentration of 100,000 cells/ml. Mitochondrial mass was assessed by flow cytometry using the FACS Canto II flow cytometer (Becton Dickingson).

Total cellular ATP measurements

SH-SY5Y cells ($2x10^5$ cells/well) were seeded in 6 well plate in glucose or galactose medium (see above); after 24 h cells were transfected with either pcDNA3 or PS2-T122R cDNAs. 24 h later, cells were washed once with PBS and detached using trypsin; cells ($1.5x10^4$ cells/well) were re-seeded in a 96-well plate in 100 μl of glucose- or galactose-containing fresh medium. 5 h later, total ATP content in each well was measured with the luciferin/luciferase assay ATPlite 1 step (PerkinElmer, 6016736), following the manufacturer's instructions. Luminescence was measured through a Fluoroskan Ascent FL Microplate Fluorimeter and Luminometer (Thermo Scientific). Where indicated, cells were treated with oligomycin (2 μM), gramicidin A (0.3 μM), UK5099 (4 μM), etomoxir (8 μM), BPTES (6 μM), ouabain (1 μM).

Luciferase ATP Measurements

SH-SY5Y cells ($0.5x10^5$ cells/well) were plated on coverslips (13 mm diameter) in glucose- or galactose-containing medium (see above); after 24 h cells were transfected with the cDNA for a mitochondrial luciferase together with either pcDNA3 or PS2-T122R or $MICU1_{EFmut}$ cDNAs and used for ATP measurements the day after transfection. Where indicated, cells were treated with either DMSO, Clotrimazole (CTM, 5 μM, 10 min), LiCl (10 mM, overnight), AR-014418 (100 nM, overnight). For Aβ treatment, the day before the experiment SH-SY5Y medium was replaced with medium collected from wt CHO or FAD-APP-V717F-expressing CHO7PA2 cells, as previously described (Hedskog et al., 2013).

HT-22 cells ($0.7x10^5$ cells/well) were plated on coverslips (13 mm diameter) in glucose- or galactose-containing medium (see above); after 24 h, before the transfection, glucose-containing medium was replaced with fresh galactose-containing medium. Cells were transfected with the cDNA for a mitochondrial luciferase together with either cytosolic-tdTomato, ΔN-HK1, FL-HK1 or Nterm-HK1 cDNAs, and with either control-siRNA or a HK1-specific siRNA; cells were then used for ATP measurements 48 h after transfection.

All the luminescence measurements were performed by transferring coverslips to the perfusion chamber and perfusing cells with different mKRB buffers (in mM: 135 NaCl, 5 KCl, 0.4 KH_2PO_4, 1 $MgCl_2$, 1 $CaCl_2$, 20 HEPES, 5 D-deoxy-glucose pH 7.4 at 37°C), supplemented as detailed below, depending on the specific protocols. Note that D-deoxy-glucose (5 mM) was added to completely block glycolysis, because FCS contain glucose (5 mM) and its addition (3%) during the experiments may otherwise activate glycolysis.

To measure mitochondrial ATP production upon ER-mitochondrial Ca^{2+} transfer stimulation, the following protocol has been used: (1) mKRB (30 s); (2) mKRB supplemented with 0.1 mM pyruvate, 1 mM lactate, 15 μM luciferin (90 s); (3) mKRB supplemented with 0.1 mM pyruvate, 1 mM lactate, 15 μM luciferin and FCS (3%, Sigma Aldrich) or Bradykinin (BK, 100 nM, Sigma Aldrich), as IP3-generating agonists. In CTM-treatment experiments, the three buffers were supplemented also with CTM (5 μM).

To measure mitochondrial ATP production upon partially depletion of ER Ca^{2+} content, the following depleting protocol was applied: (1) mKRB (30 s); (2) Ca^{2+}-free- mKRB containing 500 μM EGTA, 0.1 mM pyruvate, 1 mM lactate, 15 μM luciferin (30 s); (3) Ca^{2+}-free-mKRB containing 500 μM EGTA, 0.1 mM pyruvate, 1 mM lactate, 15 μM luciferin and 15 μM CPA (4 min); (4) same as in (3) but without CPA (100 s); (5) same as in (4) with 3% FCS.

Luminescence was collected by a photon counter (Package Photon Counting 9125, Sens-Tech) and recorded for analysis by a specific software (Sens-Tech).

Offline analysis was performed normalizing the luminescence values of the traces on the average of 25 frames before stimulations; Area Under the Curve (AUC) was calculated using Origin 7.5 SR5 (OriginLab Corporation).

FRET experiments

Cells or neurons expressing FRET probes were analyzed using a DM6000 inverted microscope (Leica, Wetzlar, Germany) and a 40X oil objective (HCX Plan Apo, NA 1.25). Excitation light, produced by a 405 nm LED (Led Engin #LZ1-00UA00 LED), was filtered at the appropriate wavelength (425 nm) through a band pass filter, and the emitted light was collected through a beam splitter (OES s.r.l., Padua, Italy) (emission filters HQ 480/40M (for CFP) and HQ 535/30M (for YFP); dichroic mirror 515 DCXR). All filters and dichroics were from Chroma Technologies (Bellow Falls, VT, USA). Images were collected using an IM 1.4C cool camera (Jenoptik Optical Systems) attached to a 12-bit frame grabber. Synchronization of the excitation source and the cool camera was performed through a control unit run by a custom-made software package, Roboscope (developed by Catalin Dacian Ciubotaru at VIMM, Padua, Italy).

Exposure time was 200 ms. Images were acquired every 5 s for ATeam1.03 probes, 2.5 s for the MPC1-CFP/MPC2-YFP couple to evaluate the assembly/functionality of MPC, 2 s for cytosolic Pyronic, 0.5 s for MIMS- and matrix-Pyronic to evaluate the kinetic of pyruvate uptake. During the experiments, cells were mounted into an open-topped chamber and maintained/treated as indicated.

Basal ATP levels measurements with FRET-based ATP probes (ATeam1.03; Imamura et al., 2009): SH-SY5Y or MEFs cells ($8x10^5$ cells/well) were seeded on 18 mm coverslips in galactose-containing medium (see above) and after 24 h they were transfected with either pcDNA3, PS2-N141I or PS2-T122R together with both H2B-ATeam1.03 (nuclear) and 4mt-ATeam1.03 (mitochondrial) cDNAs.

The experiments were performed in mKRB (in mM: 135 NaCl, 5 KCl, 0.4 KH_2PO_4, 1 $MgCl_2$, 1 $CaCl_2$, 20 HEPES, 10 mM galactose, pH 7.4 at RT).

Primary cortical neurons were grown in BME supplemented with B27 (2%), L-glutamine (0.5 mM) and Sodium Pyruvate (0.23 mM). At 5-6 DIV neurons were transfected with both H2B- and 4mt-ATeam1.03 cDNAs and the day after transfection ATP measurements were performed. Experiments were carried out in mKRB (in mM: 140 NaCl, 2.8 KCl, 2 $MgCl_2$, 10 HEPES and 1 Sodium Pyruvate pH 7.4 at RT). Where indicated, EGTA (50 μM) and Gramicidin (0.3 μM) were added.

For all the experiments, FRET ratios (calculated as YFP/CFP fluorescence emission) where transformed into FRET percentage, considering minimum (0% FRET) and maximal (100% FRET) ratios for both nuclear and mitochondrial ATeam1.03 probes, obtained as following described. SH-SY5Y cells, expressing either the nuclear or the mitochondrial ATeam1.03 probe, where permeabilized in a digitonin (25 μM)-containing intracellular-like medium (in mM): 130 KCl, 10 NaCl, 1 KH_2PO_4, 1 $MgSO_4$, 20 HEPES, 0.05 EGTA (pH 7-for the nuclear probe- or pH 8-for the mitochondrial probe- at RT). For the mitochondrial probe, ADP (500 μM) was added to favor the complete ATP extrusion from mitochondria. FRET ratios obtained in these conditions (i.e., in the absence of ATP) were considered as the minimum values (0% FRET). Then, a saturating ATP concentration (10 mM) was added to get the maximal FRET ratios of the probes (100% FRET) and calibrate all the experiments.

Pyruvate levels measurements with FRET-based pyruvate probes: SH-SY5Y and HT-22 cells ($8x10^4$ cells/well) were seeded on 18 mm coverslips in glucose-containing medium (see above) and after 24 h they were transfected with pcDNA3 or PS2-T122R together with either cytosolic Pyronic (San Martín et al., 2014), MIMS- or matrix-targeted Pyronic cDNAs and with either control- or HK1-specific siRNA. Measurements were performed in mKRB (in mM: 135 NaCl, 5 KCl, 0.4 KH_2PO_4, 1 $MgCl_2$, 1 $CaCl_2$, 20 HEPES, 10 glucose pH 7.4) at RT. Where indicated, specific drugs were added (UK5099 (4 μM); AR-C155858 (1.5μM)). To transform FRET ratio values into FRET %, minimum FRET ratio for each pyronic probe (0% FRET) was obtained from experiments performed in SH-SY5Y cells, bathed in a medium without any substrate and in which glycolysis was inhibited by 5 mM D-deoxy-glucose (to inhibit pyruvate synthesis and get the minimun FRET value). Maximal FRET ratio (100% FRET) was obtained by adding to the experimental buffer a saturating pyruvate concentration (2 mM).

Offline analysis of FRET experiments was performed with ImageJ (Wayne Rasband, Bethesda, USA). YFP and CFP images were background subtracted and distinctly analyzed after selecting proper regions of interest (ROIs) on each cell; subsequently, a ratio between CFP and YFP emissions was calculated.

For FRET experiments with the MPC1-CFP/MPC2-YFP couple, SH-SY5Y cells, seeded on 18 mm coverslips and transfected with both MPC1-CFP and MPC2-YFP plasmids (0.3 μg/each), together with pcDNA3 or PS2-T122R cDNAs (1.4 μg), were bathed in mKRB without substrates (in mM: 135 NaCl, 5 KCl, 0.4 KH_2PO_4, 1 $MgCl_2$, 1 $CaCl_2$, 20 HEPES, pH 7.4) at RT. Where indicated, pyruvate (1 mM) or Clotrimazole (CTM, 5 μM) where added. Basal FRET ratios (between the YFP and CFP fluorescence signals, corrected for crosstalk between the two channels, essentially as previously described (Palmer and Tsien, 2006; Zal and Gascoigne, 2004) were measured before pyruvate addition, to evaluate MPC1-CFP assembly with MPC2-YFP. The activity of the assembled MPC1-CFP/MPC2-YFP hetero-complexes was evaluated calculating the fold-increase of the FRET ratios (R/R0) upon pyruvate addition, i.e., normalizing the FRET ratio (R) observed at specific time points to the basal ratio measured before pyruvate addition (R0), thus taking into account that different amounts of hetero-complexes are formed between control and FAD-PS2-expressing cells. The

same calculation was performed to evaluate the effects of CTM addition on MPC1-CFP/MPC2-YFP assembly/activity in control cells, bathed in mKRB (in mM: 135 NaCl, 5 KCl, 0.4 KH_2PO_4, 1 $MgCl_2$, 1 $CaCl_2$, 20 HEPES, 1 sodium-pyruvate, pH 7.4 RT).

To evaluate glucose uptake, SH-SY5Y cells, grown in galactose-medium, were co-transfected with the indicated plasmids and with FLII12Pglu-700uDelta6, a previously described FRET-based glucose probe (Takanaga et al., 2008). 24 h after transfection, cells were bathed in mKRB without substrates (in mM: 135 NaCl, 5 KCl, 0.4 KH_2PO_4, 1 $MgCl_2$, 1 $CaCl_2$, 20 HEPES; pH 7.4 RT) and, where indicated, glucose (1 mM) was added. For calibration, maximal FRET signal was obtained by adding glucose (2 mM). No further increases in the FRET signal were observed by further increasing glucose concentration.

Ca^{2+} Measurements: Aequorin

SH-SY5Y cells ($0.5x10^5$ cells/well) were plated on coverslips (13 mm diameter) in galactose-containing medium (see above); after 24h, cells were transfected with mitochondrial Aequorin (either wt for experiments performed with FCS-stimulation or mutated for BK-stimulation) together with either pcDNA3 or PS2-T122R or $MICU1_{EFmut}$ cDNAs; cells were used for Ca^{2+} measurements the day after transfection.

24 h after transfection, cells were incubated at 37°C with coelenterazine (5 μM) for 1 h in the growth medium and then transferred to the perfusion chamber. All the luminescence measurements were performed with the same protocols and apparatus described above for ATP measurements with luciferase. All the aequorin experiments ended by permeabilizing cells with digitonin (100 μM) in a hypotonic Ca^{2+}-rich solution (10 mM $CaCl_2$ in H_2O) to discharge the remaining unused aequorin pool. The light signal was analyzed and converted into Ca^{2+} concentrations as previously described (Brini et al., 1995).

Ca^{2+} measurments: Fura-2

Primary cortical or hippocampal neurons ($8x10^5$ cells /well) were seeded on 18 mm coverslips and grown in BME medium supplemented with B27 (2%), L-glutamine (0.5 mM) and Sodium Pyruvate (0.23 mM). The experiments were performed at DIV 10-12.

Neurons were incubated with Fura-2/AM (1 μM), pluronic F-127 (0.02%), and sulfinpyrazone (200 μM) for 30-40 min at 37°C in mKRB (in mM: 140 NaCl, 2.8 KCl, 2 $MgCl_2$, 10 HEPES, 2 $CaCl_2$, pH 7.4 at 37°C), supplemented with 5 mM glucose (hippocampal neurons) or 0.1 mM Sodium Pyruvate (cortical neurons). Upon washing, coverslips were mounted in a chamber and bathed in mKRB supplemented with 5 mM glucose (hippocampal neurons) or either 0.1 mM Sodium Pyruvate or 1.5 mM Methyl-Pyruvate (cortical neurons). Fura-2–loaded cells were visualized by a 20X or 40X ultraviolet-permeable objectives (Olympus Biosystems GmbH, Planegg, Germany) on an inverted microscope (Zeiss Axiovert 100, Jena, Germany). Alternated excitation wavelengths of 340 and 380 nm were obtained by a monochromator (polychrome V, TILL-Photonics) controlled by a specific software (Roboscope). A neutral density filter, UVND 0.6 (Chroma, USA), was used in the excitation pathway. The emitted fluorescence was measured at 500–530 nm. Images were acquired every 5 s, with 200 ms exposure time at each wavelength, by a PCO SensiCam QE (Kelheim, Germany) camera controlled by the same software. Regions of interest, corresponding to the entire soma, were selected for Ca^{2+} imaging.

Hippocampal neurons

Where indicated, cells were challenged with 30 mM KCl. Cells were evaluated for their ability to recover cytosolic [Ca^{2+}] 20 min after KCl addition, grouping them into 3 different assemblies for R (F340/380): < 0.5 (low-responding); 0.5-1 (medium-responding) or > 1 (high-responding), respectively.

Cortical neurons

Where indicated, cells were challenged with 0.5 μM glutamate and evaluated for their ability to recover cytosolic [Ca^{2+}] 15 min after glutamate addition, grouping them into 3 different assemblies for R (F340/380): < 0.5 (low-responding); 0.5-1 (medium-responding) or > 1 (high-responding), respectively.

Preparation of protein extracts, Western Blot analysis and ELISA

SH-SY5Y and HT-22 cells, transfected and treated as indicated, as well as primary cortical or hippocampal neurons, were washed once with PBS; cells were then collected, using a cells scraper, in RIPA buffer (50 mM Tris, 150 mM NaCl, 1% Triton X-100, 0.5% deoxycholic acid, 0.1% SDS, protease and phosphatase inhibitor cocktails (Roche), pH 7.5). Cortices were collected from 6 month old mice and homogenized with RIPA buffer using a Potter (Sigma Aldrich). Homogenates were incubated on ice for 30 min, centrifuged at 13000 x g for 15 min at 4°C and the supernatant was collected. Proteins concentration was measured by BCA assay kit (EuroClone). 40 μg of proteins were loaded onto polyacrylamide gels (8-12%–15%) and immunoblotted as previously described (Filadi et al., 2018).

After overnight primary antibody incubation, secondary specie-specific HRP-coupled antibodies (BioRad) have been used.

The proteins were visualized by the chemiluminescent reagent ECL (Amersham, GE Healthcare) or LiteAblot TURBO (EuroClone) on an Uvitec Mini HD9 (Eppendorf) apparatus. The intensity of the bands was analyzed using ImageJ software program.

Protein stability assay was performed by blocking, for the indicated time frames, protein synthesis and/or proteasome activity with cycloheximide (50 μg/ml) or MG132 (10 μM), respectively, added directly to the growth medium.

To evaluate Aβ42 levels in the conditioned medium from wt CHO and CHO7PA2 cells, the medium was collected after 24 h and Aβ42 was measured with a specific ELISA (Wako, 292-64501), following manufacturer instructions.

Co-immunoprecipitation

SH-SY5Y cells ($2x10^6$), co-transfected with MPC1-FLAG, MPC2-MYC and with either pcDNA3 or PS2-T122R cDNAs, were washed with PBS and lysed in immunoprecipitation buffer (in mM: 20 Tris-HCl, 150 NaCl, 0.5 EDTA, 5% glycerol, 0.5% ultrapure digitonin, proteases inhibitor cocktail), as previously described [65]. Lysates were centrifuged (15000 *rcf.* x 15 minutes) and the proteins content of supernatant was quantified (BCA assay). 600 μg of protein/sample were incubated overnight at 4°C on a rocker platform with 1.5 μg of either α-MYC, α-FLAG or irrelevant mouse IgG (negative control) and then processed essentially as previously described (Filadi et al., 2018). Briefly, samples were adsorbed by adding 25 μL of protein A/G PLUS Agarose (Santa Cruz, sc-2003) at 4°C for 3 h, centrifuged (900 *rcf.*) and washed 4 times with 0.1M NaCl plus protease inhibitors, finally re-suspended by incubating with 50 μL of Loading Buffer at 60°C for 10 min. Proteins were separated by SDS-PAGE and probed with the indicated antibodies.

BNE Gel and Sample Preparation

Pellets of mitochondria were suspended at 10mg/mL in 0.75 M aminocaproic acid and 50 mM Bis-Tris, pH 7.0 (Giorgio et al., 2009), solubilized with 2.4%–5% (wt/vol) digitonin, and immediately centrifuged at 100,000 *rcf.* for 25 min at 4°C. The supernatants were supplemented with Coomassie Blue G-250 (Serva) and rapidly applied to 1D 4%–11% polyacrylamide gradient blue-native electrophoresis (Galber et al., 2019). After electrophoresis, proteins were stained with Silver staining, or transferred to a PVDF membrane for Western Blot analysis (Galber et al., 2019).

Oxygen Consumption Rate (OCR) and ECAR measurements in living cells

SH-SY5Y cells ($1x10^4$ cells/well) were seeded in 250 μL of galactose-containing medium (see above) in XF24 cell culture microplates (Seahorse Bioscience) and transfected after 24 h with either pcDNA3 or PS2-T122R cDNA. 24 h after transfection, the medium was replaced with 670 μL of mKRB (in mM: 135 NaCl, 5 KCl, 0.4 KH_2PO_4, 1 $MgCl_2$, 1 $CaCl_2$, 20 HEPES, pH 7.4 at 37°C) supplemented with either 10 mM galactose, 0.1 mM pyruvate or 2 mM methyl-pyruvate. For the experiments with pyruvate and methyl-pyruvate, 30 mM HEPES, instead of 20 mM, was added to mKRB, to avoid pH changes during the measurements. Cells were incubated at 37°C for 30 min, and then OCR was measured with an XF24 Extracellular Flux Analyzer (Seahorse Bioscience). After OCR baseline measurement, specific drugs were added as indicated (oligomycin-A (1 μg/ml); carbonyl cyanide-4-(trifluoromethoxy)phenylhydrazone (FCCP, 0.5 μM); UK5099 (4 μM); Etomoxir (8 μM); BPTES (6 μM); rotenone (0.1 μM); antimycin A (1 μM); 3-nitropropionic acid (3NPA, a complex II inhibitor; 10 mM). After the experiments, cells were counted and data were normalized for cell number and further normalized to control baseline OCR. For ECAR measurements, cells were bathed in mKRB (in mM: 135 NaCl, 5 KCl, 0.4 KH_2PO_4, 1 $MgCl_2$, 1 $CaCl_2$, 20 HEPES, 2 glucose; pH 7.4 at 37°C). After baseline measurements, glucose (10 mM), oligomycin-A (1 μg/ml) and D-deoxy-glucose (20 mM) were added. ECAR was calculated for basal glycolysis (baseline measurements subtracted of the values obtained after D-deoxy-glucose addition), glycolysis (values obtained during glucose addition (10 mM) subtracted of those observed after D-deoxy-glucose addition) and glycolytic capacity (values obtained after oligomycin-A addition subtracted of those obtained after D-deoxy-glucose addition). Values were normalized for cell number and to control baseline.

Mitochondrial Transmembrane Potential Measurements in living cells

Mitochondrial membrane potential ($\Delta\Psi$) was detected by tetramethyl rhodamine methyl ester (TMRM) fluorescent dye.

SH-SY5Y ($2x10^5$ cells/well) were seeded on 24 mm coverslips in galactose-containing medium (see above); after 24 h, cells were loaded for 45 min at RT with 10 nM TMRM, in mKRB (in mM: 135 NaCl, 5 KCl, 0.4 KH_2PO_4, 1 $MgCl_2$, 1 $CaCl_2$, 20 HEPES, 10 galactose pH 7.4 at RT).

Primary hippocampal neurons (DIV 10-12) were incubated for 30 min at 37°C in mKRB (in mM: 140 NaCl, 2.8 KCl, 2 $MgCl_2$, 10 HEPES, 2 $CaCl_2$, 5 glucose, pH 7.4 at 37°C), supplemented with 10 nM TMRM and 2 μg/ml Cyclosporin H (CsH) to inhibit multidrug-resistance pumps, which could affect TMRM loading.

TMRM fluorescence was recorded using an inverted microscope (Zeiss Axiovert 100) with a 40X oil objective (Fluar, NA 1.30). Excitation light at 540 ± 7.5 nm was produced by a monochromator (polychrome V; TILL Photonics) and passed through a Zeiss TRITC filter (Emission 573-613 nm) and a dichroic mirror (565 DCXR). Images were acquired by a cooled CCD camera (SensicamQE PCO). Filters and dichroics were from Chroma Technologies. Images were collected every 60 s (50 ms exposure). Where indicated, oligomycin-A (1 μM), clotrimazole (5 μM), rotenone (2 μM) and Antimycin-A (1 μM) were added. At the end of each experiment, 3-10 μM FCCP was added to assess the correct distribution of the dye. Images were exported as TIFF, background subtracted and analyzed with ImageJ.

Immunofluorescence (IF) and confocal analysis

Cells, transfected and treated as indicated, were first washed once with PBS and then fixed in 4% PFA in a PBS solution (supplemented with 0.1 g/ml sucrose for neurons). After 15 min in PFA, cells were washed 3 times (3 × 5 min) in PBS and then quenched 20 min with NH_4Cl (50 mM in PBS). Cells were then permeabilized for 3 min with 0.1% Triton X-100 in PBS and blocked with a PBS solution containing 2% BSA, 10% goat serum and 0.2% gelatin for 30 min.

Cells were incubated with primary antibodies diluted in blocking solution (dilution 1:200 for HK1; 1:200 cytochrome-c) for 1.5 h at RT and washed three times (3 × 5 min) with the blocking solution. Cells were then incubated for 45 min at RT with

AlexaFluor488/555-conjugated secondary antibodies (Life Technologies; 1:300 dilution in blocking solution). Coverslips were washed 3 times (3 × 5 min) with the blocking solution and then with PBS (10 min); finally, they were mounted with Mowiol.

For BODIPY C12 staining, SH-SY5Y cells were grown in galactose-containing medium, transfected with a mitochondrial-CFP encoding plasmid and incubated ON with BODIPY C12 (Thermo Scientific, D3835, 2 μM) and with or without etomoxir (8 μM, to inhibit CPT1 activity and thus lipid transfer to mitochondria), as previously described (Rambold et al., 2015). 24 h after transfection, cells were bathed in mKRB (in mM: 135 NaCl, 5 KCl, 0.4 KH_2PO_4, 1 $MgCl_2$, 1 $CaCl_2$, 20 HEPES, 10 galactose; pH 7.4 at RT) and imaged.

Images were collected with a Leica SP5 confocal system (DM IRE2) using a WLL white laser (Leica). Each channel was collected independently, and photomultiplier gain was maintained among different experiments to minimize background and avoid saturation. Once acquired, images were background subtracted and not modified further before co-localization analysis. However, the signal intensity of representative images was enhanced automatically with specific ImageJ plugins (*Adjust Brightness*), to better appreciate low fluorescent signals. Co-localization analysis was performed for each cell using ImageJ *Colocalization* plugins, essentially as previously described (Filadi et al., 2016). To calculate the mean fluorescence intensity of the different probes (reported in Table S1), ROIs including the whole cell areas were traced. For each experiment, fluorescence values were normalized to those of the controls. Where indicated, linear ROIs were traced within cells and the fluorescent signals for red and green channels were plotted to evaluate signal co-distribution.

Drugs

Ciclopiazonic acid (CPA, Abcam biochemical ab120300); Gramicidin-A (Abcam, ab144510); UK-5099 (Sigma Aldrich, PZ0160); oligomycin-A (Sigma Aldrich, 75351); carbonyl cyanide-4-(trifluoromethoxy)phenylhydrazone (FCCP, Sigma Aldrich C2920); Clotrimazole (Sigma Aldrich, C6019); rotenone (Sigma Aldrich, R8875); antimycin-A (Sigma, A8674);AR-C155858 (Tocris bioscience, 4960); AR-A014418 (Sigma, A3230); Methyl-Pyruvate (Sigma Aldrich; 371173); Etomoxir (Sigma Aldrich, E1905); BPTES (SigmaAldrich, SML0601); Digitonin (Calbiochem, 300410); MG132 (Sigma Aldrich, M8699); cycloheximide (Sigma Aldrich, C7698).

Antibodies

Mouse anti-actin (A4700; Sigma-Aldrich); rabbit anti-AMPK (Cell Signaling, 2532S); rabbit anti-Phospho-AMPK (Thr172, Cell Signaling, 2531S); mouse anti-cytochrome *c* (Cell Signaling, 12963); rabbit anti-GSK3 α/β (Cell Signaling, 5676); rabbit anti-phospho Y216/Y279 GSK3 α/β (Abcam, ab4797); rabbit anti-HK1 (Thermo Scientific Pierce, #MA5-14789); rabbit anti-MPC1 (D2L9I, Cell Signaling, 14462); rabbit anti-MPC2 (D4I7G, Cell Signaling, 46141); rabbit anti-OXPHOS MitoProfile (MS604, MitoSciences); mouse anti-tubulin (Santa Cruz Biotech, sc-53646); mouse anti-TIM23 (BD Biosciences, 611222); mouse anti-MYC (Millipore, 05-724); rabbit anti-MYC (Cell Signaling, 2278); mouse anti-FLAG (Sigma Aldrich, F3165); rabbit anti-FLAG (Sigma Aldrich, F7425); mouse anti-tubulin (Santa Cruz Biotech, sc-5286); rabbit anti-phospho-PDH (Millipore, ABS204); mouse anti-PDH (Santa Cruz Biotech, sc-377092).

QUANTIFICATION AND STATISTICAL ANALYSIS

All data are representative of at least 3 different experiments, as detailed in figure legends. Data were analyzed using Origin 7.5 SR5 (OriginLab Corporation) and ImageJ (National Institutes of Health). Significance was calculated by unpaired Student's t test for normally distributed data or Wilcoxon rank-sum test for data not following normal distribution. Normality was tested by Shapiro-Wilk test. Unless otherwise specified, numerical values presented throughout the text refer to mean ± SEM (* = $p < 0.05$, ** = $p < 0.01$, *** = $p < 0.001$).

DATA AND CODE AVAILABILITY

This study did not generate any unique datasets or code.